Eur. Phys. J. D **35**, 279–297 (2005)
DOI: 10.1140/epjd/e2005-00199-0

THE EUROPEAN PHYSICAL JOURNAL D

Electron-driven processes in high-pressure plasmas

K.H. Becker[1,2,a], N.M. Masoud[1,b], K.E. Martus[3], and K.H. Schoenbach[4,5]

[1] Dept. of Physics and Engineering Physics, Stevens Institute of Technology, Hoboken, NJ, USA
[2] Center for Environmental Systems, Stevens Institute of Technology, Hoboken, NJ, USA
[3] Dept. of Chemistry and Physics, William Paterson University of New Jersey, Wayne, NJ, USA
[4] Dept. of Electrical and Computer Engineering, Old Dominion University, Norfolk, VA, USA
[5] Center for Biolelectrics, Old Dominion University, Norfolk, VA, USA

Received 9 March 2005 / Received in final form 21 May 2005
Published online 26 July 2005 –

Abstract. This review article summarizes results from selected recent studies of collisional and radiative processes initiated and driven by low-energy electron interactions with atoms and molecules in high-pressure plasmas. A special emphasis of the article is on spectroscopic studies of plasmas used as sources for non-coherent vacuum ultraviolet radiation such as rare excimer emissions and atomic and molecular emissions from plasmas in admixtures of rare gases and the molecular gases H_2 and N_2. An attempt is made to correlate the various observed emission features and their dependence on the plasma operating parameters (pressure, power, gas mixture, mode of excitation, etc.) to the underlying microscopic atomic and molecular processes.

PACS. 33.80.-b Photon interactions with molecules – 34.80.-i Electron scattering – 52.20.-j Elementary processes in plasmas

1 Introduction

Discharge plasmas at high pressures, where single collision conditions no longer prevail, provide a fertile environment for the study of collisions and radiative processes dominated by (i) step-wise processes, i.e. the excitation of excited states followed by collisions of the excited species with other particles resulting in new energy transfer routes and by (ii) three-body collisions leading e.g., to the formation of excimers. The dominance of collisional and radiative processes beyond binary collisions involving ground-state species allows for many applications of high-pressure plasmas such as high power lasers, opening switches, novel plasma processing applications and sputtering, electromagnetic (EM) absorbers and reflectors, remediation of gaseous pollutants, medical sterilization and biological decontamination, and excimer lamps and other non-coherent vacuum-ultraviolet (VUV) light sources [1]. However, self-sustained diffuse discharges tend to be unstable at high pressure due to their susceptibility to filamentation and the transition to an arc (see [2,3] and references therein to earlier work), which limits their practical utility.

Several approaches have been developed to generate and maintain stable glow-type discharge plasmas at elevated pressures. In the past few years, we have studied the properties of three stable atmospheric-pressure plasmas and their utility in various applications, the micro-hollow cathode discharge (MHCD), the capillary plasma electrode discharge (CPED), and a cylindrical dielectric barrier discharge (C-DBD). The non-equilibrium, high-pressure plasmas generated in these devices were used in many applications, for instance as efficient sources of VUV atomic line radiation and excimer sources [4], for the treatment of Diesel exhaust [5], and for H_2/CH_4 generation for fuel cells [6,7]. In addition, we worked on the remediation of gaseous pollutants [8], biological decontamination [9], and the cleaning of metallic surfaces [10]. The technological applications of high-pressure discharge plasmas have outpaced the detailed understanding of the plasma physics and the key processes on an atomic and molecular level. Furthermore, these plasmas, when excited with electrical pulses of microsecond (or shorter) duration, were found to exhibit improved technologically useful properties (enhanced UV and VUV emission, enhanced and selective production of chemically reactive radicals, etc.), for which there is no satisfactory detailed basic scientific understanding. Electron-driven processes are the key to achieving a microscopic understanding and ultimately control of the processes that determine the properties of these high-pressure discharge plasmas.

In this topical review, we describe some recent results of our studies of the VUV emissions from MHCDs, CPEDs, and C-DBDs in pure rare gases and in mixtures

[a] e-mail: kbecker@stevens-tech.edu
[b] *Present address*: U.S. Army, TACOM/ARDEC, Picatinny Arsenal, NJ, USA.

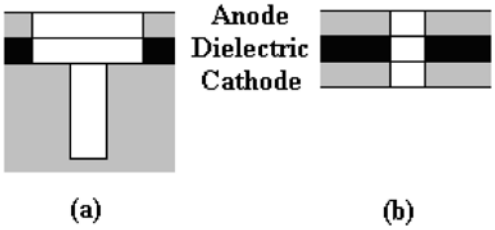

Fig. 1. Electrode geometries for microhollow cathode discharges (MHCDs).

of rare gases with trace amounts of H_2, N_2, and air. The emissions are primarily rare gas excimer emissions and H, N, and O atomic line emissions. We also present results of measurements of rotational and vibrational temperatures in these plasmas. As will be shown, a detailed understanding of collision physics is critical to the interpretation of these measurements.

2 Background

2.1 Basic aspects of MHCDs, CPEDs, and C-DBDs

2.1.1 Microhollow cathode discharges (MHCDs)

Hollow cathode (HC) discharges are gas discharges between a cathode with a hollow structure and an arbitrarily shaped anode. A typical HC structure consists of a cylindrical hole in a cathode with a ring shaped anode, separated by a dielectric spacer (Fig. 1a) [11], or the anode can just be a metal pin [12]. The cathode "hollow" can also be a cylindrical opening in a thin cathode layer (Fig. 1b) [13]. Modeling results [14] and experiments [15] for discharges in such geometries at gas pressures, p, and cathode hole diameters, D, such that the product (pD) is on the order of 1 Torr cm, show various discharge modes. For very low currents, the discharge extends from the cathode surface through the cathode hole to the anode. The electric field in the cathode hole is axial. With increasing current, the plasma column formed along the axis of the cathode hole begins to serve as a virtual anode that modifies the electric field distribution in the cathode hole. The initially axial electric field in the cathode plane changes into a radial one, and electrons generated at the cathode are accelerated radially towards the axis. For pressures such that the diameter of the cathode opening is twice the cathode fall plus the length of the negative glow or less the electrons accelerated in the cathode fall reach the opposite cathode fall, where they are again accelerated and oscillate with ever decreasing amplitude between the opposite cathode falls. The increased ionization rate of such "pendulum" electrons in the hollow cathode causes a decrease in voltage at constant current, or an increase of current at constant voltage (negative differential conductance, hollow cathode effect). With further increasing current, the cathode layer expands over the surface of the planar cathode outside the hole. The I-V characteristic becomes that of a normal glow discharge with constant voltage at increasing current. Ultimately, when the cathode layer reaches the boundaries of the cathode, any further current increase requires an increase in discharge voltage: the discharge changes to an abnormal glow discharge.

Assuming that the HC effect is caused by "pendulum" electrons, HC discharges are expected to follow a similarity law [12,13,15,16]: $V = V(pD)$, with V being the sustaining voltage for the HC discharge. The similarity law for HC discharges is the basis of efforts to extend the pressure range for HC discharge operation to atmospheric pressures. By using cathodes with holes of diameter D, down to the ten micron range it is possible to operate HC discharges at atmospheric pressure. However, it was shown experimentally, that stable MHCDs can be obtained at atmospheric pressure in rare gases even when the hole diameter is on the order of 100 μm. For these conditions the effects attributed to the "hollow cathode effect" (I-V characteristics with negative differential resistivity) cannot be due to pendulum electrons because the electron energy loss mean free path is too short to allow electrons emitted from one part of the cathode to reach the opposite sheath with enough energy to ionize. The negative differential region can according to new modeling results [17] be associated with a transition from a glow discharge localized inside the hollow cathode to a glow discharge spreading along the outer cathode surface. Thus, the steep slope of the I-V characteristic at low current corresponds to an abnormal glow discharge inside the hollow cathode; increasing current is achieved by increasing the current density. Above a certain current, enough ions (and metastables) from the HC discharge reach the outer surface of the cathode to initiate a discharge between the outer cathode surface and the anode. Once initiated, this discharge is sustained by ions and metastables created mainly in the volume outside the HC. This second discharge is in parallel with the first discharge inside the HC, and the I-V characteristic above a certain current reflects the behavior of the normal glow discharge along the outer cathode surface.

Most of our MHCD studies used the electrode geometry shown in Figure 1b because of its simplicity, which allows easy manufacturing of large-area micro-electrode arrays by plasma spraying and laser drilling [18] and the possibility to flow gas through the discharge volume inside the hollow. The latter is advantageous for thermal management (cooling of electrodes) and for the replenishment of gas, contaminated by sputtered or evaporated electrode material. Stable glow discharges with dimensions up to centimeters, even in atmospheric pressure air, could be generated [19]. The electrodes used for plasma cathodes and for excimer source studies described in the following consist of two molybdenum foils, with circular openings, separated by a dielectric film, generally 100–250 μm thick alumina (Al_2O_3). The cylindrical holes in the cathode and the dielectric range between 80 μm and 700 μm. The discharges were either operated dc or pulsed, with pulse durations either in the ms range or in the ns range. The ms pulses with duty cycles of 0.007 allowed us to increase the peak power without increasing the average power and,

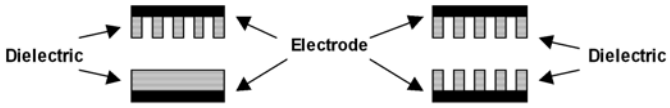

Fig. 2. Schematic diagram of a capillary plasma electrode discharge (CPED) configuration.

consequently, enhance the power without causing thermal damage to the sample. Nanosecond pulsing increases the electron energy with negligible gas heating [20].

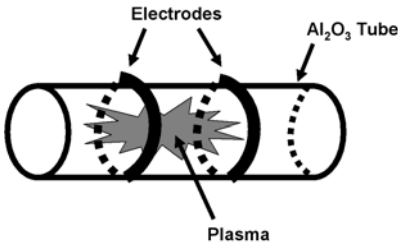

Fig. 3. Schematic diagram of a cylindrical dielectric barrier discharge (C-DBD) configuration.

2.1.2 Capillary plasma electrode discharges (CPEDs)

The operating principles and properties of the capillary plasma electrode discharge (CPED) (Fig. 2) are much less well understood and researched. The basis for the atmospheric-pressure operation of the CPED is a novel electrode design [21] that uses dielectric capillaries that cover one or both electrodes of the discharge device. The capillaries, with diameters from 0.01 to 1 mm and length-to-diameter, L/D ratios of about 10:1, serve as plasma sources which produce jets of high-intensity plasma at atmospheric pressure. The plasma jets emerge from the end of the capillary and form a "plasma electrode" for the main discharge plasma. The CPED displays two distinct modes of operation when excited by pulsed dc or ac. When the frequency of the applied voltage pulse is increased above a few kHz, one observes first a diffuse mode similar to the diffuse glow described of a DBD as described by Okazaki and co-workers [22]. When the frequency reaches a critical value (which depends strongly on the L/D value and the feed gas), the capillaries "turn on" and a bright, intense plasma jet emerges from the capillaries. In addition to the detailed description of the CPED in our three US patents [21], further information regarding this discharge concept can be found in several publications [3,5–10,23–25]. The "capillary" mode is the preferred mode of operation and has been characterized in a rudimentary way for several lab-scale research discharge devices in terms of peak discharge current (2 A), current density (up to 80 mA/cm^2), E/p (0.25 V/(cm Torr)), and electron density n_e (10^{13} cm^{-3}). We note that these are only approximate values because of the inhomogeneous nature of the plasmas generated in these devices. Using a Monte Carlo modeling code [25,26], the existence of the threshold frequency has been verified. The model also predicts relatively high average electron energies of 5–6 eV in the "capillary" mode. By paralleling a large number of capillaries, it is possible to obtain a nearly uniform discharge.

2.1.3 Cylindrical dielectric barrier discharges (C-DBDs)

Dielectric barrier discharges (DBDs) are characterized by solid insulating layers on one or both electrodes. Usually, DBDs at atmospheric pressure consist of many tiny current filaments. Homogeneous discharges can be obtained under special circumstances [22]. In the filamentary mode, the discharge in a DBD device starts with local gas breakdown at many points in the discharge volume. The breakdown in a DBD and the formation of microdischarges has been thoroughly studied and is well-understood [27]. The discharge sequence encompasses 4 phases. The initial breakdown at high electric fields is called the Townsend phase. Subsequently, the streamer or ionization phase leads to the formation of a highly conducting channel (filament) with a diameter of about 0.1 mm and a current density of up to 100 A/cm^2. Charges are transferred through this channel and accumulate on the dielectric surface (phase 3) until the voltage across the filament is compensated and the discharge dies out (phase 4). The time scale for the completion of a full 4-cycle discharge development is of the order of a few nanoseconds. Conditions in a filament are: electron densities up to 10^{15} cm^{-3}; average electron energies up to 20 eV, particularly in the streamer head; gas temperatures near room temperature. However, these conditions exist only in a filament, i.e. on a ns time scale and in small spatial volumes. Averaged over the entire discharge volume, the average electron energy is much lower (below 1 eV, albeit with a pronounced high-energy tail) and the electron density is only of the order of 10^{10} cm^{-3}. Current and voltage traces of homogeneous DBDs [22] show a sequence of μs-long pulsed discharges with one pulse per half cycle of the exciting AC voltage. The microscopic mechanisms that cause a uniform DBD plasma are the subject of intense current studies and are still not completely understood. The discharge parameters that can be realized in a homogeneous DBD are closer to the average discharge parameters in a filamentary DBD and do not reach the extreme parameters (in terms of electron density and electron temperature) in a filament.

In addition to the commonly used parallel-plate and annular DBD configurations, Laroussi [28] introduced a cylindrical geometry (C-DBD) where both electrodes are on the outside of a dielectric tube and the plasma is generated inside the tube and confined to the space between the two electrodes as shown in Figure 3. This geometry has the advantage that the plasma is not in direct contact with the electrodes and electrode erosion is avoided. We have studied alumina (Al_2O_3) C-DBDs excited by rf power with tube diameters in the range of a few millimeters and electrode separations up to a few centimeters [29–31].

2.2 Excimer formation

Rare gas molecules exist only in the form of excimers (*exci*ted di*mers*), which are characterized as having repulsive ground states that are dissociative and bound excited states. Transitions from the bound excited states of a rare gas excimer to the repulsive ground state results in continuous emissions. Rare gas excimer emission spectra are dominated by the so-called second continuum which corresponds to transitions from the lower vibrational levels of the lowest lying bound $^3\Sigma_u$ excimer state to the repulsive ground state with peak emissions at 170 nm (Xe), 145 nm (Kr), 130 nm (Ar), 84 nm (Ne), and 75 nm (He). The so-called first excimer continua in the rare gases are observed on the short-wavelength side of the second continua and are due to the radiative decay of vibrationally excited levels of the $^1\Sigma_u$ excimer state. In Ne, the second excimer continuum covers the wavelength range from 76–88 nm, whereas the first excimer continuum appears as a narrow feature centered between 73–75 nm [32–34].

The most common routes to rare gas excimer formation are via electron-impact ionization

$$e^- + \mathrm{X} \rightarrow \mathrm{X}^+ + 2e^- \quad (1a)$$

$$\mathrm{X}^+ + 2\mathrm{X} \rightarrow \mathrm{X}_2^+ + \mathrm{X} \quad (1b)$$

$$\mathrm{X}_2^+ + e^- \rightarrow \mathrm{X}^* + \mathrm{X} \quad (1c)$$

$$\mathrm{X}^* + 2\mathrm{X} \rightarrow \mathrm{X}_2^* + \mathrm{X} \quad (1d)$$

where X = He, Ne, Ar, Kr, or Xe and the asterisk denotes a metastable rare gas atom, or alternatively directly via excitation of metastable rare gas atoms by electrons

$$e^- + \mathrm{X} \rightarrow \mathrm{X}^* + e^- \quad (2a)$$

$$\mathrm{X}^* + 2\mathrm{X} \rightarrow \mathrm{X}_2^* + \mathrm{X}. \quad (2b)$$

Minimum electron energies required for excimer formation range from 11–14 eV in Xe to 20–24 eV in He. In the ionization route, reaction (1c) is usually the rate-limiting process, as this dissociative recombination process has a cross-section as a function of electron energy which exhibits a narrow peak at energies close to zero. In either case, the excimer molecules are formed in three-body collisions involving a metastable rare gas atom and two ground-state atoms. The final 3-body reaction in pure xenon Xe* + Xe + Xe → Xe_2* + Xe has a rate constant of 5×10^{-32} cm^6/s at room temperature [35]. The excited excimers decay radiatively into a repulsive ground state, so that reabsorption is negligible and the plasma and excimer gas is optically thin for excimer radiation. Efficient excimer formation requires (i) a sufficient number of electrons with energies above the threshold for the metastable formation (or ionization), and (ii) a pressure that is high enough for 3-body collisions to be important. MHCDs, CPEDs, and C-DBDs are known for electron energy distributions with a high concentration of energetic electrons. Electron energies well over 10 eV were measured or inferred from spectroscopic studies in MHCDs [32]. All three discharges at high pressure emit intense excimer radiation. The efficiency of excimer formation is highly susceptible to quenching of the rare gas metastables, the precursors of the excimers. Metastable rare gas atoms (with the exception of He) have natural radiative lifetimes of about 1 s [36]. If the frequency of quenching collisions is comparable to or larger than the frequency for 3-body collisions leading to the formation of excimers, most metastables are quenched before they can form an excimer molecule resulting in a low excimer formation efficiency.

Furthermore, small concentrations of impurities are detrimental for excimer sources. It is important to use highly purified gases, evacuate the discharge chamber before operation, and use materials for the discharge chamber with low gas emission. A way to overcome the contamination problem is to work with flowing gas. On the other hand, impurities such as O_2 have a place as VUV line emission sources. Small additions of O_2 to Ar at high pressure allowed us to increase the O line emission at 130.5 nm, at the expense of excimer emission, to values of 13 mW at discharge currents of 10 mA [37]. The excimer efficiency (i.e. the ratio of optical output power to the electrical input power) was measured to be 6% in flowing Ar [38], which is slightly less than that obtained for Xe (8% for dc operation [39]), but higher than what was obtained for ArF and XeCl excimers (1% and 3%, respectively [40,41]). For all the gases, the excimer emissions were found to increase linearly with current at constant voltage (normal glow) and constant pressure [42]. The intensity (power/area), on the other hand, which in Xe at 760 Torr was measured to be 2 W/cm^2, is independent of the discharge current in the normal glow mode [43,44]. Modeling results and experiments in high pressure glow discharges [20] showed that the application of sub-microsecond pulses allows electron heating without considerable gas heating. By applying pulses of 20 ns duration with voltages up to 750 V to a Xe MHCD, the excimer emission could be increased up to 2.75 W at an intensity of 15 W/cm^2 and the efficiency reached almost 20% [45].

3 Experimental set-ups

We will restrict the description of the experimental set-ups to those two set-ups that were used in our spectroscopic studies in the near-ultraviolet/visible (UV-VIS) and in the vacuum ultraviolet (VUV) region of the spectrum involving the C-DBD device (for more detailed descriptions of the experimental set-ups, we refer the reader to references [29–31]). Briefly, our C-DBD source consists of a $1/4''$ (approximately 0.635 cm) diameter dielectric tube (alumina, Al_2O_3) and two straps of Cu wrapped around it, separated by a distance of 2.5 mm, which serve as the two electrodes. A 13.56 MHz rf source delivers up to 100 W at a few hundred Volts to the electrodes to generate and sustain a stable discharge plasma inside the tube which is roughly confined to the space between the two electrodes. Figure 4 illustrates the experimental set-up used in the UV-VIS studies. The feed gas or gas mixture is introduced into the tube through a precision leak valve and the gas flow is controlled by flow meters. In

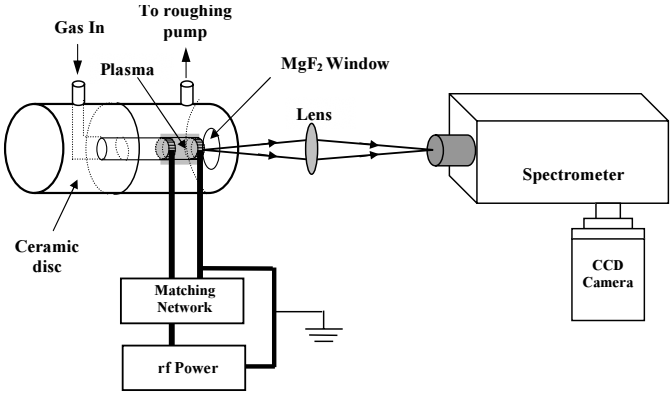

Fig. 4. Experimental set-up for the measurement of rotational and vibrational temperatures and the near-UV spectroscopy.

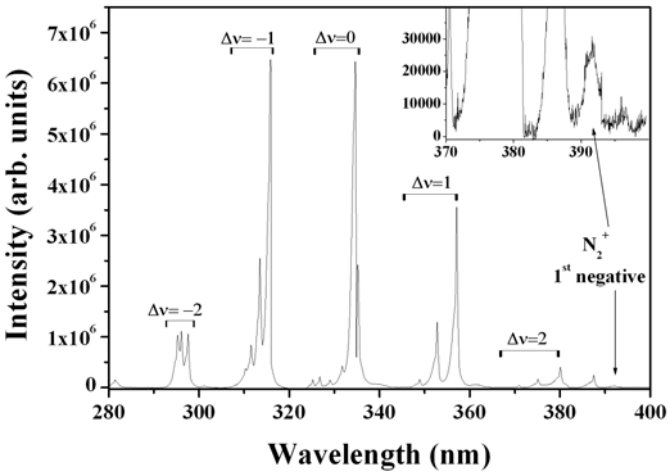

Fig. 5. A typical emission spectrum in the range of 280–400 nm from the C-DBD source operated in pure N_2 at a pressure of 10 Torr and a net rf power of 20 W.

order to maximize the power that the rf generator delivers into the plasma, a matching network was used to match the impedance of the plasma (load) with the output impedance of the generator. The optical emissions were analyzed using a scanning monochromator with variable entrance and exit slits (SPEX Model 1710) in conjunction with 1024×256 pixel CCD detector (Roper Scientific I-MAX – 1024). To optimize the collection of light, a lens of focal length $f = 7.5$ cm was used to focus the light from the source onto the entrance slit of the monochromator. The source was positioned in such a way that the light was collected from the center of the tube. Emission spectra were recorded in the wavelength range from 200–400 nm. The emissions from the N_2 2nd positive system are recorded and used to determine the rotational and vibrational temperatures as described below.

For the VUV studies, we replaced the UV-VIS detection system with a Minuteman 302-V 0.2 m VUV spectrometer with a McPherson XUV-2025 CCD camera to detect photons in the wavelength range from 50–150 nm. Since the Ne resonance line radiation and the Ne_2^* excimer emission are in the 70–100 nm range, where no material transmits optical radiation, a windowless arrangement between the plasma source and the vacuum monochromator/detector system had to be used. The system is differentially pumped using multiple pumping stations to maintain a reduced pressure inside the vacuum monochromator and the CCD camera. The pressure inside the CCD camera never exceeded 10^{-5} Torr, when the gas pressure inside the discharge chamber varied from 1 to 600 Torr. For the studies of the Ar excimer emissions and the emissions from Ar–N_2, Ar–air, Ne–N_2, and Ne–air mixtures, which all occur above 120 nm, we removed the differential pumping stages and mounted the plasma source, which was sealed with a Mg_2F window, directly onto the entrance slit of the VUV monochromator.

We used a different set-up in our time-resolved emission spectroscopic studies from MHCD plasmas. The MHCD device was mounted directly onto the entrance slit of the VUV monochromator and the neon excimer radiation from the MHCD entered the VUV monochromator through a 0.2 mm pinhole between the discharge region and the monochromator, which is differentially pumped to provide an operating pressure in the 10^{-5} Torr range in the detector chamber. The VUV photons were detected by a channel electron multiplier connected to a standard pulse counting system. Time-resolved fluorescence spectra of the Ne_2^* excimer emission were recorded with a SR400 gated photon counting system controlled by a PC. In these studies, we used a MHCD device with electrodes made of 0.1 mm thick molybdenum foils, which are separated by a 0.25 mm spacer of mica with a hole of typically 0.1–0.2 mm diameter in the cathode, the dielectric, and in the anode. The MHCD was excited in a pulsed dc mode with pulses of peak voltages of several hundred volts and up to 25 mA, pulse widths from 50 ns to 20 μs and repetition rates in the kHz range.

4 Results and discussion

4.1 Rotational and vibrational temperature measurements

In an effort to characterize the high-pressure microplasma in terms of the rotational and vibrational temperatures of the plasma species, we added a small amount of N_2 (<0.05%) to the discharges in pure Ne (or Ar). A typical emission spectrum in the range of 280–400 nm from our C-DBD operated in pure N_2 at a pressure of 10 Torr and a net rf power of 20 W is shown in Figure 5. The most prominent vibrational bands are due to the N_2 2nd positive system ($C\ ^3\Pi_u \rightarrow B\ ^3\Pi_g$) and have been labeled in Figure 5. The (0,0) band of the N_2^+ 1st negative system ($B\ ^2\Sigma_u^+ \rightarrow X\ ^2\Sigma_g^+$) can also be seen in the spectrum at 391.4 nm. When we replace pure N_2 with the typical Ne+N_2(0.02%) mixture, the emissions attributed to the N_2^+ 1st negative system essentially disappear and the N_2 2nd positive system remains the only emission feature that can be observed with appreciable intensity. The presence of the N_2 2nd positive system and the absence of the N_2^+

1st negative system in our high-pressure Ne–N_2(0.02%) plasma is a consequence of the low concentration of N_2. In addition, the N_2^+(B) state is also very efficiently quenched in our plasma by collisions with N_2, Ne, and by dissociative recombination. These non-radiative decay processes are in direct competition with the radiative decay of the N_2^+(B) ions and may also contribute to the fact that we did not see any appreciable emissions of the N_2^+ 1st negative system from our Ne–N_2 mixture.

4.1.1 Rotational temperature measurements

One reason for using the N_2 second positive system for the determination of rotational temperatures (and gas temperatures) in plasmas is the fact that this band system is readily observed in discharge as long as there is a trace of N_2 in the discharge gas mixture. Furthermore, the molecular constants describing this transition are well-known [46], so that the synthetic model spectra can be calculated easily and with high accuracy. Assuming that the emitting N_2 molecules can be described by a Maxwell-Boltzmann distribution characterized by a single rotational temperature T_R, this temperature can be determined from a fit of the measured emission spectrum, usually from a single, isolated vibrational band, to a synthetic spectrum with T_R as the only free parameter. This can be accomplished, for instance, by recording the fully rotationally resolved structure of the band (i.e. by recording the emission intensity of the individual rotational lines of the band) and by fitting the intensities of the rotational lines to a "rotational Boltzmann factor" (Boltzmann plot [47–49]) from which one can obtain T_R. As an alternative to recording fully rotationally resolved spectra, one can record the unresolved envelope of vibrational band with high statistical accuracy and then obtain T_R from a "best-fit" of the envelope of the measured spectrum to a calculated band envelope, again with the rotational temperature as the only free parameter. However, the calculation of the band envelope requires the convolution of the calculated intensity of each rotational line with a monochromator slit function, which must determined with high precision in a separate experiment using a narrow atomic line emission.

In the present study we determined rotational temperatures for N_2(C) molecules in our C-DBD plasma in Ne–N_2(0.02%) mixtures from the a rotational analysis of the unresolved N_2 band system. Details of the data acquisition and analysis procedure have been described before in the papers by Masoud et al. [30] and Kurunczi et al. [50], to which we refer the reader for further details. Only the main points will be reiterated here briefly. The calculation of the line intensities for the synthetic spectra of the N_2 second positive system is straightforward [48] using the molecular constants as reported by Laux and Kruger [46]. For the calculation of the unresolved band envelopes, each rotational line was convoluted with an appropriate monochromator slit function. Figure 6 illustrates the comparison between a measured spectrum and three calculated spectra corresponding to different rotational temperatures. We selected the (1,2) vibrational band of the N_2 second positive system at 353.7 nm, which is well isolated from adjacent emission features, emitted by a C-DBD discharge in a 400 Torr mixture of Neon with 0.02% N_2 at a power of 30 W. The three synthetic spectra in Figure 6 correspond to rotational temperatures of 250 K, 357 K, and 450 K. The comparison in Figure 6 shows that the calculated spectrum (using the portion of the band from 351.5–354.5 nm) corresponding to a rotational temperature of 357 K provides a good fit to the measured spectrum, whereas the spectra corresponding to a rotational temperature of 450 K and 250 K clearly overestimate the short wavelength part (450 K) or the long wavelength part (250 K) of the band. We always carried out a "chi-squared", χ^2, analysis for each recorded spectrum by minimizing the relative χ^2 value with respect to T_R (χ^2 is defined as $\chi^2 = \sum[y_i - y(x_i;T_R)]^2$ ($i = 1, 2, 3 \ldots N$) where y_i denotes the measured intensity at the ith wavelength position, $y(x_i;T_R)$ refers to the calculated intensity at the same wavelength position for a fixed T_R, and the sum extends over all data points from 1 to N). From the χ^2 analysis we found that the uncertainty in the determination of the rotational temperature is typically ±15 K.

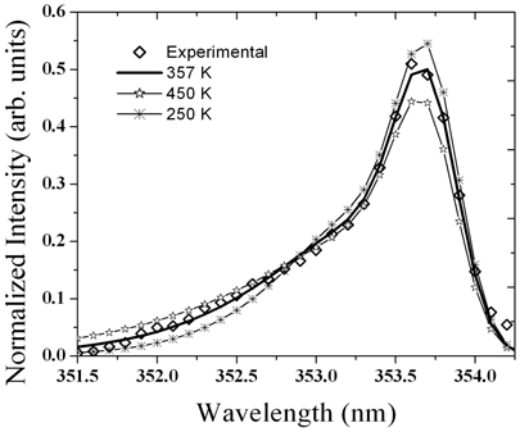

Fig. 6. Comparison between a measured spectrum of the (1,2) band of the N_2 second positive system and three calculated spectra corresponding to different rotational temperatures (250 K, 357 K, and 450 K). The various spectra were normalized to one another at a wavelength of 352.9 nm.

Figure 7 shows the rotational temperature of the N_2 (C $^3\Pi_u$) state as a function of pressure from 200 Torr to 600 Torr at a constant rf power of 30 W. The rotational temperature stays essentially constant at around 360 K (within the margin of uncertainty) between 200 and 600 Torr. The N_2 (C $^3\Pi_u$) state is efficiently produced via direct electron impact excitation of ground-state N_2 atoms and via "pooling" reactions involving the collision of two metastable N_2(A $^1\Sigma_u^+$) atoms. The N_2 (C $^3\Pi_u$) state has a natural radiative lifetime of 37 ns [51], which is considerably reduced in our plasma by quenching through collisions with primarily N_2 molecules and to a lesser extent with Ne atoms. Taking into account — as a function of pressure — the apparent lifetime of the N_2(C) state,

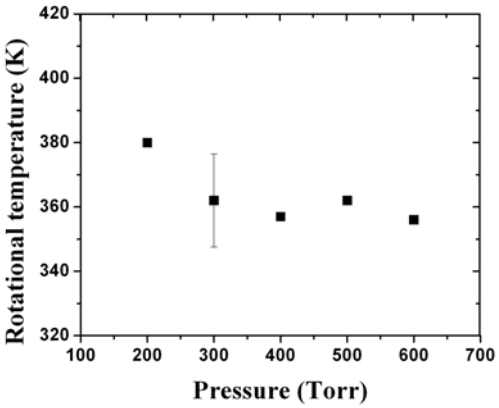

Fig. 7. The rotational temperature as a function of pressure from 200 to 600 Torr at a constant rf power of 30 W.

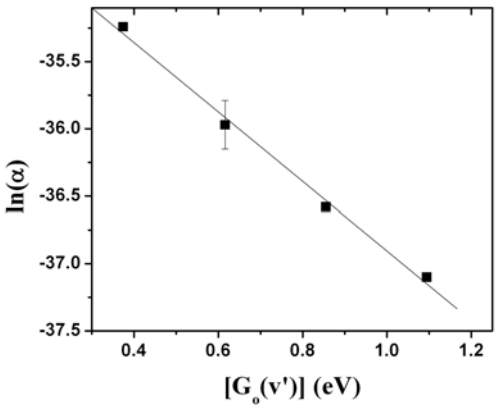

Fig. 8. A semi-log plot of the scaled intensity α of a sequence of vibrational bands (with $\Delta v = -1$ as shown in Fig. 2) of the 2nd positive system vs. the energy of the vibrational level above the $v' = 0$ level, $G_o(v')$. Here the parameter α represents the emission intensity divided by the product of wave number and Einstein transition probability. The slope of the straight line allows the determination of the vibrational temperature (see text for details).

the collision frequency of the $N_2(C)$ molecules, and the rotational relaxation time [52], we find that the $N_2(C)$ molecules at pressure above about 200 Torr are in thermodynamic equilibrium with the background gas and thus can be equated with the gas temperature. We note that the gas temperatures determined here at pressures above 200 Torr are slightly higher than room temperature and are comparable to gas temperatures measured in other high-pressure non-equilibrium plasmas such as microhollow cathode discharge and capillary plasma electrode plasmas [50].

As a function of power, we observed an essentially linear increase of the gas temperature from 340 K at 25 W to about 390 K at 60 W (at a constant pressure of 400 Torr). This is not unexpected and confirms earlier observations in other high-pressure discharge plasmas [53,54]. The temperature rise is attributed to a (slight) gas heating as the power input into the plasma increases. Above 60 W, we observe a sudden jump in the gas temperature, which coincides with a noticeable change in the visual appearance of the plasma and a dramatic increase in the emission intensity from the plasma in the vacuum ultraviolet spectral region [29]. A similar observation has been reported by other authors [54] in other discharge plasmas.

4.1.2 Vibrational temperature measurements

The determination of the vibrational temperature, T_v, requires the analysis of the several vibrational bands that belong to a given electronic transition and that differ in the vibrational quantum number v' (upper vibrational level) and v'' (lower vibrational level). A detailed discussion of the T_v determination can be found in the paper by Masoud et al. [30] as well as in references given in that paper. The basic procedure involves plotting the scaled recorded emission intensity of a sequence of vibrational bands (with $\Delta v =$ constant) of the 2nd positive system as a function of the energy of the vibrational level above the $v' = 0$ level, $G_o(v')$, on a semi-log scale. This plot yields a straight line, whose slope allows the determination of the vibrational temperature. This is shown in Figure 8 for

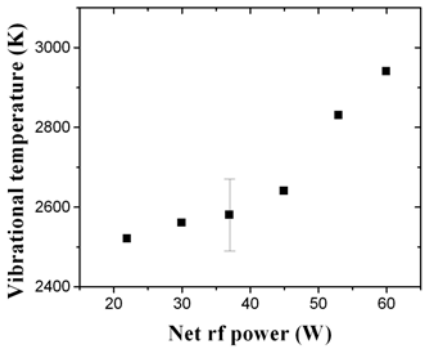

Fig. 9. The vibrational temperature as a function of the rf power at a pressure of 400 Torr.

the sequence $\Delta v = -1$ (1-0, 2-1, 3-2, 4-3) of the 2nd positive system of N_2 at 315.93, 313.6, 311.67, and 310.4 nm. The molecular constants and the transition probabilities have been taken from references [48,55–57]. Similar plots were used to determine the vibrational temperatures of the Ne+N_2 (or air) systems for a variety of plasma conditions (pressure, power, concentration and frequency). The vibrational temperatures in our plasma were found to vary from 2270–5850 K depending of the discharge conditions as discussed below. The uncertainty of the measurement of the vibrational temperature is estimated to be ±4%.

As a function of pressure, we found that the vibrational temperature decreased as the pressure increased from 3030 K at 200 Torr to 2270 K at 600 Torr (at a constant power of 30 W). This decrease of T_v with increasing pressure is attributed to a combination of the enhanced collisional relaxation of the vibrationally excited N_2 levels as the collisional frequency increases with pressure and a decrease of the electron temperature with pressure. The vibrational temperature increases with the rf power as shown in Figure 9 (at a pressure of 400 Torr). This

dependence mimics the power dependence of the rotational temperature. However, the increase of T_R with pressure was attributed to an increase in the gas heating at higher powers, whereas the increase of the vibrational temperature with increasing power is a consequence of the increase in the average electron energy with the power. An increase in the average electron energy means that higher vibrational levels are more efficiently excited by the plasma electrons [58] and hence the vibrational temperature will increase.

4.2 VUV emissions from rare gas plasmas

In this section we discuss primarily the VUV emission in the 50–200 nm wavelength range from high-pressure C-DBD and MHCD plasmas in pure Ne and Ar and in gas mixtures that contain small admixtures of H_2, N_2, or air (N_2/O_2 mixtures). The various emissions are characterized and an attempt is made to correlate their variations with pressure, power, gas flow rate, and other plasma operating parameters with the collisional and radiative processes in the plasma, in particular with electron-initiated and electron-driven processes. We also present some results from near-UV studies in the 320–370 nm wavelength region from a low-pressure pure Ne plasma. This spectral region is rich in emission lines from neutral and singly ionized neon.

4.2.1 UV/VUV emissions from rf-excited Ne C-DBD plasmas

Non-equilibrium plasmas in pure Ne emit a wide range of spectral features from the far VUV to the near-infrared. The spectral region in the near-UV between 320 nm and 370 nm is particularly rich in emission lines from both neutral Ne (Ne I lines) and singly ionized Ne (Ne II lines). All emission lines in this region are attributed to transitions between high-lying excited states of Ne or Ne^+. Minimum energies required for exciting the emitting Ne levels from the Ne ground state are above 20 eV, whereas minimum energies for populating the emitting levels of Ne^+ are about 30–38 eV above the Ne ground state or 9–17 eV above the Ne^+ ground state.

Figure 10 shows the power dependence of the emission intensity of three Ne lines (342 nm, 352 nm, 359 nm) and three Ne^+ lines (335 nm, 338 nm, 357 nm) from a pure Ne plasma at 3 Torr. As can be seen, the Ne line intensities increase linearly between 4 W and 35 W, whereas the increase of the Ne^+ intensity follows is quadratic with power. At the comparatively low pressure of 3 Torr, electron-driven excitation (and ionization) of neutral neon proceeds primarily through electron interactions with ground state Ne, while step-wise processes involving excitation and ionization of Ne metastables are comparatively insignificant. Since the three NeI lines terminate in short-lived lower states that quickly decay radiatively to the Ne ground state, the main route for populating the emitting neutral Ne levels is via direct excitation of Ne ground state

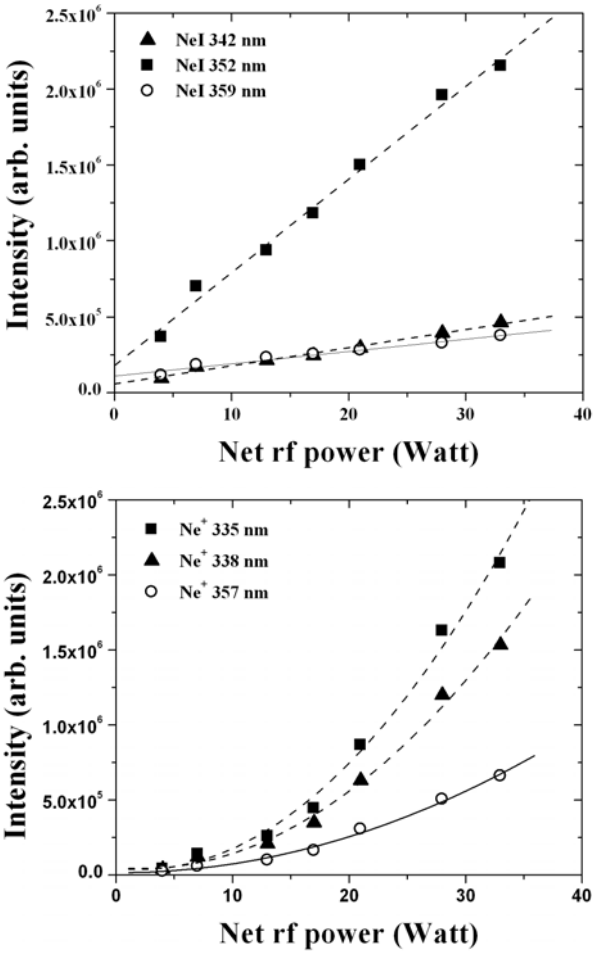

Fig. 10. Power dependence of selected Ne and Ne^+ lines emitted by a 3 Torr C-DBD plasma in pure Ne.

atoms. Thus, the observed linear increase in their intensity with increasing power reflects the increase in electron density and electron temperature as the power deposited into the plasma is increased. By contrast, the emitting levels of the Ne^+ ions can be populated directly by electron-driven ionization excitation of neutral Ne ground-state atoms, or alternatively by electron excitation of ground-state Ne^+ ions, which themselves are the result of electron-driven ionization of ground-state Ne atoms in the plasma. The observed quadratic dependence of the Ne^+ emission lines on the power (and thus on the electron density and electron temperature) suggests that the latter two-step process is the dominant route. The former single-step ionization-excitation of Ne would result in a linear power dependence, similar to what was observed for the neutral Ne lines.

The most prominent VUV emissions that are observed from a low-pressure Ne plasma are the Ne resonance lines at 73.59 nm and 74.37 nm, which arise from radiative transitions from respectively the excited "$^1P_1$" and "$^3P_1$" states to the $^1S_0$ ground state. The quotation marks indicate that the excited states cannot be described in an LS angular momentum coupling scheme, but are more appropriately described in an intermediate angular

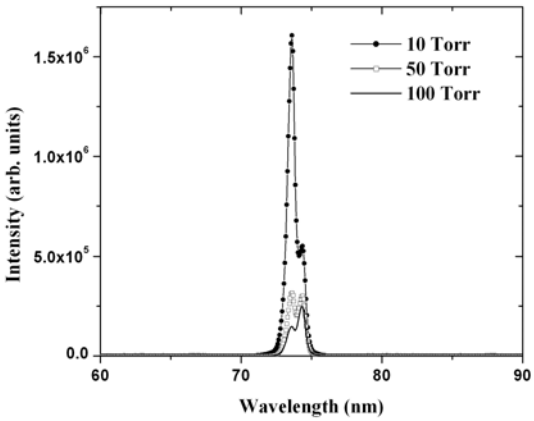

Fig. 11. Low-pressure spectrum of a neon discharge at 10, 50 and 100 Torr in the 60–90 nm region. The net rf power is 30 W and the gas flow rate is 800 sccm. The lines connecting the data points are just a guide to the eye.

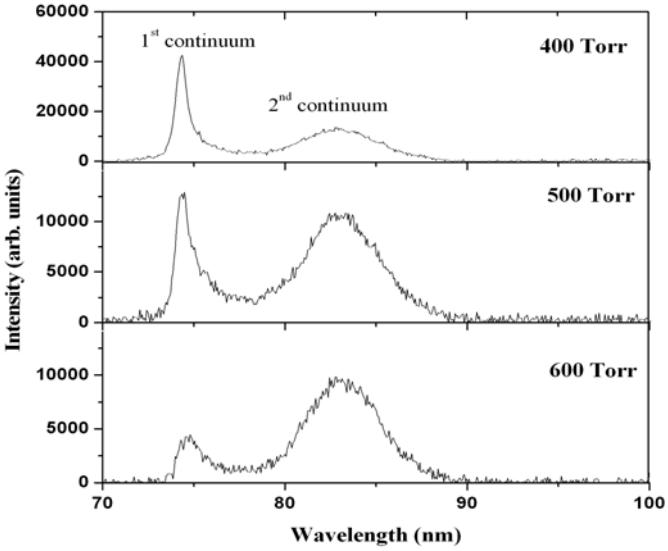

Fig. 12. High-pressure spectrum of a neon discharge at 400, 500 and 600 Torr. The net rf power is 30 W and the gas flow rate is 800 sccm.

momentum coupling scheme [59]. Alternatively, the excited "$^1P_1$" and "$^3P_1$"states of the rare gases are often described as mixtures of LS-coupled singlet and triplet states and the radiative decay of both states proceeds through the singlet component. The singlet-triplet mixture depends on the particular excited states and the particular rare gas atom [60]. In Ne, the first excited singlet state has about a 10% triplet admixture and vice versa [61]. The natural lifetime of the "$^1P_1$" and "$^3P_1$" states are 1.87 ns and 31.7 ns, respectively [62]. As the pressure in a Ne plasma increases, molecular excimer emissions begin to appear.

Figure 11 shows the emission spectrum of a pure neon discharge in the wavelength range from 60–90 nm obtained at pressures of 10, 50, and 100 Torr. These spectra are dominated by the Ne resonance lines. There is no indication in the spectra of Ne excimer emissions. At these low pressures the rate for three-body collisions involving metastable Ne atoms, which would lead to excimer formation, is much smaller than rates for two-body collisions that cause quenching of the Ne metastables. Thus, the radiative decay of the "$^1P_1$" and "$^3P_1$" is the dominant process.

The ratio of "singlet" (73.6 nm) to "triplet" (74.6 nm) emission intensity changes dramatically as a function of pressure. At 10 Torr, the 73.6 nm line is about 3 times as intense as the 74.6 nm line. At 50 Torr, the intensity of the lines are roughly equal. However, the overall intensity at 50 Torr is lower than the overall intensity at 10 Torr. At 100 Torr, both lines are much weaker and the 74.6 nm line is now more intense than the 73.6 nm line by about a factor of 2. This change in the emission intensity with pressure is a consequence of self-absorption and radiation trapping of the Ne resonance radiation, which affects the 73.6 nm line to a much larger extent because of its higher transition probability. We lastly note, that even at a pressure of 10 Torr, significant radiation trapping and quenching occurs as the intensity ratio of the two lines when excited by electron impact at very low pressure, i.e. under single collision conditions is close to 17.

At pressures above 200 Torr, we find no discernible evidence of the presence of the Ne resonance lines in the spectrum obtained from our source and the Ne_2^* excimer emissions in the 70–90 nm region become the dominant feature. This is due to the fact that the rate for three-body collisions involving Ne metastables leading to excimer formation begins to dominate over the rates for two-body quenching collisions. Figure 12 shows the emission spectra obtained from a pure Ne discharge (at a net power of about 30 W and a gas flow rate of 800 sccm) for pressures of 400, 500, and 600 Torr. The spectra are dominated by the narrow first excimer continuum peaking at a wavelength of about 74 nm and by the broad second excimer continuum, which covers the wavelength region from 76 nm to 88 nm with a peak emission at about 84 nm.

The emission intensity of the first excimer continuum decreases monotonically by more than a factor of 25 as the pressure increases from 200 Torr to 600 Torr [29]. By contrast, the emission intensity of the second continuum increases by about 30% as the pressure is increased from 200 Torr to 400 Torr [29]. However, as the pressure is increased further, the emission intensity of the second continuum also decreases as discussed by Masoud et al. [29]. The pressure dependence of the two Ne_2^* excimer emission continua is similar to what was observed by other authors investigating Ne_2^* excimer emissions from a variety of sources such as high-pressure Ne gas excited by energetic electron or ion impact [62,63] and other high-pressure discharge plasmas including DBDs and microhollow cathode discharges [27,64,65]. All groups reported a dominant first excimer continuum at pressures below about 400 Torr, which is quenched very efficiently at pressures above 400 Torr. For higher pressures, the emission spectrum is dominated by the second continuum, whose overall emission intensity peaks around 400 Torr and declines gradually as the pressure is increased further. This can be understood

from the detailed microscopic analysis of the excimer formation where the decay of the upper vibronic states proceeds through two pathways, collisional de-excitation to low-lying vibronic states of the excimer and radiatively to the dissociative ground state. The vibrational relaxation process to the lower-lying vibronic states depends on the collision frequency (i.e., pressure). Therefore, at low pressure the collision frequency is low and the vibrational relaxation time is large, so that the dominant decay process is radiative to the ground state leading to the emission of the first continuum. If the pressure increases, the collision frequency increases, the relaxation time for the collisional pathway decreases, and the lower-lying vibronic states are populate and subsequently decay to the ground state emitting the second continuum. The decline in the intensity of the second continuum at higher pressures (>400 Torr) is attributed to the fact that, at these pressures, the gas density is very high, so that both the excited Ne atoms, which are the precursor of the Ne_2^* excimer, and the excimer molecules are quenched.

As a function of power deposited in the plasma, the intensity of the first continuum increases more or less monotonically as the power goes up. The intensity of the second continuum increases almost linearly between 15 W and 50 W, but then levels off for higher powers. The increase in the excimer emission intensity with increasing power corresponds to an increase in the electron density and a shift in the average electron energy to higher values. Thus, an increase in power leads to an increase in the rate of metastable Ne formation, which are the precursors of the Ne_2^* excimers.

An increase of the Ne gas flow rate causes very little change in the emission intensity of the first continuum (which is almost independent of the flow rate), but a distinct increase of the intensity of the second continuum. A possible explanation for this behavior is the fact that the flowing gas carries away impurities. The intensity of the second excimer continuum is particularly sensitive to quenching collisions with impurities because of the long radiative lifetime of the emitting state. Thus, reducing the impurities by increasing the flow rate will result in less efficient quenching and an increase in the intensity of the second continuum.

In addition to the prominent first and second Ne excimer continua, there is also a third continuum, which has been observed by other authors [63,66,67], mainly following bombardment of high-pressure rare gases by energetic electron or ion beams. Even though the third continuum has rarely been observed in high-pressure rare gas discharge plasmas, we established a range of operating parameters of our rf C-DBD plasma in Ne, for which the third continuum can be observed. At a pressure between 200 Torr and 250 Torr and at comparatively low power, the Ne_2^* third excimer continuum appears at wavelengths between 92 and 105 nm as shown in Figure 13. The origin of the third continuum is still a subject of debate. Langhoff [67] assigned the third excimer continuum to an emission associated with the radiative decay of the doubly charged Ne_2^{2+} ion into two singly charged Ne ground-state atoms. Amirov [68] proposed a highly-excited singly charged rare gas ion as the origin of the third continuum emission. It is interesting to note that the emission of the third continuum from our source could only be observed in a narrow pressure range (200–250 Torr). This is similar to an observation by Leichner [62], who found a broad continuum emission peaked at around 100 nm at a pressure around 100 Torr, which disappeared at 500 Torr in their experiments.

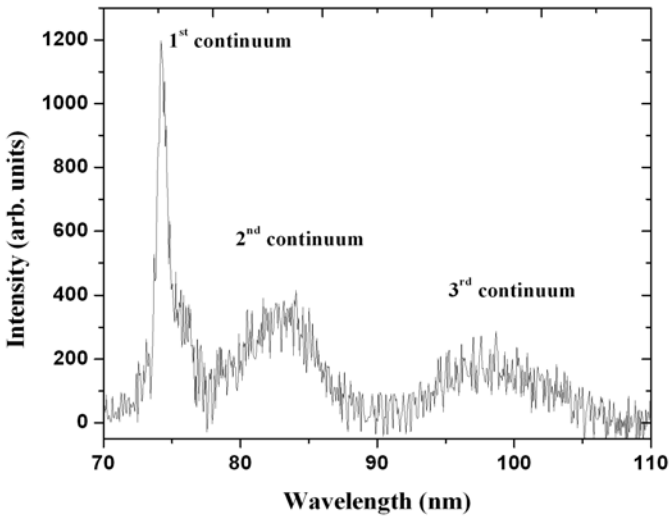

Fig. 13. Third Ne excimer continuum shown in the emission spectrum of a Ne discharge (pressure 250 Torr, gas flow rate 800 sccm, and net rf power 15 W).

4.2.2 VUV emissions from pulsed MHCD plasmas in Ne

Schoenbach and co-workers [45] reported a significant increase in the xenon excimer emission intensity following pulsed dc excitation of a MHCD plasma in pure Xe. We carried out time-resolved emission spectroscopic studies of the Ne_2^* excimer emission following pulsed excitation of a MHCD plasma in pure Ne. A detailed analysis of the time-resolved fluorescence spectra allows insight into the microscopic processes that govern the Ne_2^* excimer formation and decay processes.

Figure 14 shows the time-resolved emission of the Ne_2^* excimer from a MHCD plasma in 420 Torr Ne following pulsed dc excitation (dashed line). The diagram also depicts the discharge current pulse (solid line) that ignites the MHCD plasma. The point $t = 0$ in Figure 14 was chosen arbitrarily in a way that the figure conveniently displays the entire timing sequence of the experiment. As the discharge current rises to its maximum value of about 4 mA on a time scale of 5 μs, the excimer emission slowly increases and reaches a steady-state intensity after about 8 μs indicating that the excimer formation increases with increasing discharge current as one would expect. After both the discharge current and the excimer emission intensity reach their steady-state values, the current pulse is turned off. Almost immediately, the excimer emission intensity in the afterglow begins to rise sharply and reaches

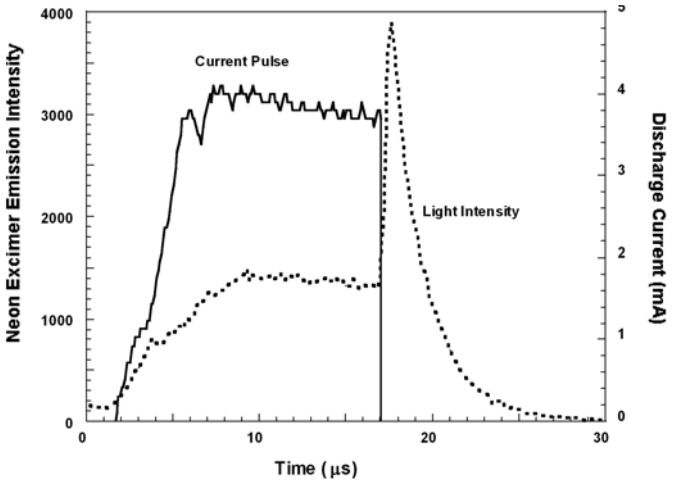

Fig. 14. Time dependence of the current pulse (solid line) and Ne_2^* excimer emission (dashed line) following pulsed dc excitation of a MHCD plasma in Ne at 420 Torr.

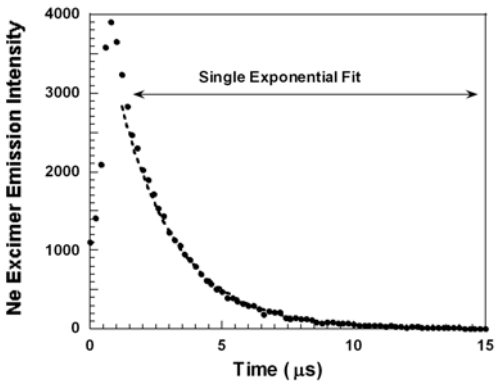

Fig. 15. Time dependence Ne_2^* excimer emission following pulsed dc excitation of a MHCD plasma in Ne at 420 Torr. The time $t = 0$ corresponds to the end of the exciting dc current pulse. The dashed line represents a single-exponential fit to the decaying part of the recorded time-resolved emission spectrum.

a peak value that is about a factor of 2.5 higher than the steady-state value during the time the current pulse was applied. We attribute this increase to a rapid cooling of the plasma electrons as the input power to the MHCD plasma is terminated. As the plasma electrons approach zero energy, the recombination step (1c), which is usually the "bottleneck" in the ionization route becomes temporarily a very efficient channel for excimer formation. Thus, the increase in the excimer formation when the exciting current is terminated, can be attributed to a temporary enhancement in the ionization route to excimer formation. Eventually, all excimer formation processes cease and the excimer emission decays exponentially as one would expect. Experiments with different current pulse widths [33] indicate that much higher excimer emission efficiencies (i.e. higher ratios of light intensity per Watt of electrical input energy) can be obtained by using pulses with a FWHM (full width at half maximum) of less than 1 μs.

It is interesting to analyze the time-resolved excimer emission intensity more quantitatively. This can be done by using the following rate equation describing the destruction of $Ne_2^*(^3\Sigma_u)$ excimers following pulsed excitation in the afterglow

$$d[Ne_2^*]/dt = -[Ne_2^*](A_{ik} + 1/k_q[Q]) \qquad (3)$$

where $[Ne_2^*]$ is the density of the Ne_2^* excimers, A_{ik} is the inverse spontaneous emission life time of the $Ne_2^*(^3\Sigma_u)$ excimer molecules (which has a value of $(8.9)^{-1}$ μs^{-1} [69]), $k_q[Q]$ is the sum of all quenching rates (collisional quenching by impurities, other losses due to e.g. wall processes, etc.) that contribute to the non-radiative decay of the $Ne_2^*(^3\Sigma_u)$ excimer molecules. As before, the time $t = 0$ was chosen to coincide with the falling edge of the exciting dc current pulse. Equation (3) results in a simple exponential decay of the Ne_2^* emission intensity with a decay constant $1/\tau$ given by

$$1/\tau = A_{ik} + 1/k_q[Q]. \qquad (4)$$

Figure 15 shows the analysis of the decay of the Ne_2^* excimer emission shown in Figure 14. The decay of the emission intensity is well-represented by a single-exponential fit. We obtain a decay constant which corresponds to an apparent lifetime of about 2.2 μs. This is shorter than the natural lifetime of the $Ne_2^*(^3\Sigma_u)$ excimer state (8.9 μs, see above) by a factor of 4, which. indicates that quenching processes expressed by the second term in equation (4) are very important in MHCD plasmas under these operating conditions and, in fact, represent the dominant channel of Ne_2^* excimer destruction. We found a systematic decrease in the apparent lifetime of the Ne_2^* excimer molecules in MHCD from about 2.4 μs to 1.9 μs as the pressure was increased from 250 Torr to 700 Torr. This indicates that (i) quenching rather than the radiative decay is the dominant destruction channel for the Ne_2^* excimer molecules in a MHCD plasma and that (ii) quenching and other non-radiative loss processes become more important as the pressure in the MHCD plasma increases. This makes it imperative to ensure a very high gas purity in VUV light sources that are based on MHCD plasmas in Ne (and other rare gases) and to select materials with low sputtering yields to minimize contamination of the operating gas.

4.2.3 VUV emissions from rf-excited Ar C-DBD plasmas

Figure 16 shows the emission spectrum from a discharge in pure Argon in the wavelength range from 115–180 nm obtained at pressures of 50, 150, and 300 Torr. We note that the spectrum was not corrected for the wavelength-dependent sensitivity of the detection system. At 50 Torr, the spectrum is dominated by the NI atomic line at 120 nm and strong emission bands between 140 and 175 nm. There is also a weak emission line at 130 nm, which we attribute to the OI resonance lines and a very weak indication of the Ar excimer emission around 126 nm (which also coincides with an impurity carbon line emission). At this pressure, the rate of three-body collisions involving metastable Ar

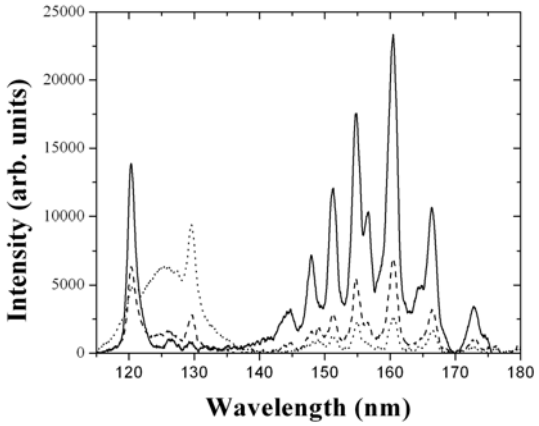

Fig. 16. Emission spectra from a "pure" Ar discharge from 115 nm to 180 nm at 3 pressures, 50 Torr (solid line), 150 Torr (dashed line), and 300 Torr (dotted line). The net rf power was 22 watts at 13.56 MHz and the flow rate was 800 sccm.

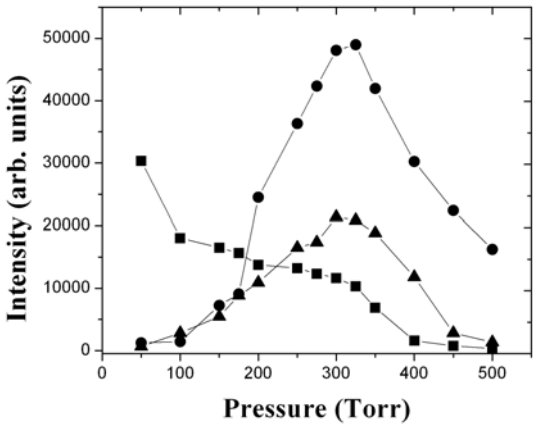

Fig. 17. Intensity (in arb. units) from a "pure" Ar discharge as a function of pressure for the N (120 nm, squares), Ar_2^* excimer (126 nm, circles), and O (130 nm, triangles) emissions at 22 Watt net rf power and 800 sccm flow rate.

atoms, which lead to excimer formation, is much smaller than the rates for two-body collisions that cause quenching of the Ar metastables. Thus, the radiative decay of the excited Ar "$^1P_1$" and "$^3P_1$" states is the dominant process. The corresponding Ar resonance line emissions at 104.8 nm and 106.7 nm cannot be detected in our system, because the MgF_2 window has a cutoff wavelength around 115 nm.

Even in "pure" Ar, the NI and OI emission lines are present, presumably arising from unavoidable traces of oxygen and nitrogen from residual moisture (water vapor), sputtering of the dielectric tube, and small air leaks. As discussed e.g. by Wertheimer [70], collisional energy transfer from the long-lived Ar^* metastables to N and O atoms are the main source of these intense atomic line emissions. The impurity emissions were also observed in many other discharges in "pure" Ar [37,71,72]. The emissions in the 140–175 nm range that we observed are similar to those found by other authors. We attribute the observed emissions in the 140–175 nm wavelength range to the N_2LBH bands corresponding to the transition a $^1\Pi_g \rightarrow X\ ^1\Sigma_g^+$ (see also Fig. 20 below and the discussion in Sect. 4.2.5).

At pressures of 150 Torr and higher, the Ar_2^* excimer emission begins to appear more prominently in the emission spectra and becomes the dominant emission feature at about 325 Torr. This is due to the fact that the rate for three-body collisions involving Ar metastables leading to excimer formation now dominates over the rates for two-body quenching collisions.

Figure 17 shows the emission intensities of the Ar_2^* second excimer continuum, the NI (120 nm) line, and the OI (130 nm) line as a function of gas pressure from 50 Torr to 500 Torr. The data represent the peak areas of each emission feature (in arbitrary units). The relative intensities of the three emission features in the 120–130 nm have not been corrected for changes in the wavelength-dependent detection sensitivity of our monochromator/detector system as stated earlier. The change in the detection sensitivity between 120 nm and 130 nm is negligible. The emission intensity of both the OI line and the Ar_2^* excimer increases initially as a function of pressure. The Ar_2^* excimer emission intensity increases by a factor of 6.7 between 150 Torr and 325 Torr, where it reaches its maximum. The intensity increase of the OI line is a factor of 3.8 in that pressure range. As the pressure is increased further, the emission intensity of both features decreases monotonically between 325 Torr and 500 Torr. By contrast, the emission intensity of NI line at 120 nm decreases essentially monotonically as the pressure increases.

The pressure dependence of the Ar_2^* excimer emission continuum is similar to what was observed previously in the case of the Ne_2^* second excimer continuum, where the emission reached its maximum intensity at 400 Torr [29]. The decrease in the Ar_2^* excimer emission intensity at pressures above 325 Torr is attributed to the fact that, at these pressures, the gas density is sufficiently high, so that quenching of both the excited Ar atoms (the precursor of the Ar_2^* excimers) and of the excimer molecules become important processes [73] and prevent a further increase of the excimer emission intensity as the pressure increases above 325 Torr. The pressure dependence of the OI atomic line emission at 130 nm is similar to that of the Ar_2^* excimer emission. This is a consequence of the fact that the O emission is the result of the reabsorption of Ar_2^* excimer photons by O atoms and thus exhibits the same pressure dependence. By contrast, the decrease of the emission intensity of the NI line at 120 nm with increasing pressure is a consequence of self-absorption and radiation trapping.

The pressure dependence of the Ar_2^* excimer emission and the OI line emission at 130 nm has been studied before in other high-pressure discharge plasma [37,72,73]. These authors reported a correlation similar to what was observed here and referred to it generically as an "energy transfer process" between the Ar_2^* excimer and the O atoms. We prefer to denote this process as 'resonant reabsorption' of the Ar_2^* excimer photons by O atoms. This is done in an effort to clearly distinguish this

process (which involves O atoms that result from the dissociation of O_2 in the plasma) from the previously described [29,64,74] "near-resonant energy transfer" between Ne_2^* excimers and H_2 molecules in high-pressure discharge plasmas in Ne–H_2 mixtures. In this process, a single-step near-resonant energy transfer between Ne_2^* and H_2 causes the dissociation of H_2 into a ground-state ($n = 1$) H atom and an excited ($n = 2$) H atom which subsequently decays radiatively emitting H Lyman-α radiation. As was shown by Kurunczi et al. [4], the appearance of the H Lyman-α line in the emission spectrum coincides with a dramatic decline in the Ne_2^* excimer emission. This is very different from the correlation between the Ar_2^* and OI emission intensity observed in the present study.

As the power was increased, we observed that the volume of the plasma slightly increased, thus maintaining an essentially constant power density. As a function of power (at a constant pressure of 300 Torr), the intensity of the Ar_2^* second continuum increases rapidly between 12 W and 20 W, stays essentially constant between 20 W and 30 W, and gradually decreases with increasing power above 30 W. The increase in the excimer emission intensity with increasing power is attributed to an increase in the electron density and a shift in the average electron energy to higher values with increasing power deposition into the plasma. However, very high electron densities can cause quenching of the excimers, which may contribute to the decrease in excimer emission intensity above 30 W. Perhaps even more important is the fact that an increase in power deposition into the plasma leads to an increase in the gas temperature [30], which, in turn, at constant pressure reduces the gas density and thus the rate of the three-body collisions. The intensity of the OI emission line shows the same trend as a function of power as the Ar_2^* excimer emission as one would expect. By contrast, the intensity of the NI line emission at 120 nm increases linearly with the power as a result of the increase of the electron density and average electron energy.

4.2.4 VUV emissions from a rf C-DBD plasma in a Ne–H_2 mixture

Similar to what was done before in the experiments reported by Wieser et al. [74] (e-beam excitation of a high-pressure Ne–H_2 mixture) and Kurunczi et al. [64,75] (excitation of a high-pressure Ne–H_2 mixture in a micro-hollow cathode discharge plasma), we studied the VUV emissions from the rf excited C-DBD plasma in a high-pressure Ne–H_2 mixture. The objective was to investigate the resonant energy transfer between the Ne_2^* second excimer continuum and H_2 molecules leading to the emission of a monochromatic H Lyman-α line in this device and to extend the earlier investigation of Dakrouri et al. [73] to a simultaneous analysis of the Ne_2^* excimer emission and the H Lyman-α emission. Figure 18 shows the emission spectrum from our source obtained by adding a small amount of hydrogen (0.02%) to Ne at a total pressure of 500 Torr, a total gas flow rate of 800 sccm, and a net rf power of 30 W. Compared with the previous spectrum obtained in pure Ne (Fig. 12), we see a dramatic decrease in the relative intensity of the second continuum accompanied by the emission of a very intense, monochromatic H Lyman-α line. We subsequently studied the dependence of the H Lyman-α emission intensity on the pressure, the net rf power, the gas flow rate, and the H_2 concentration.

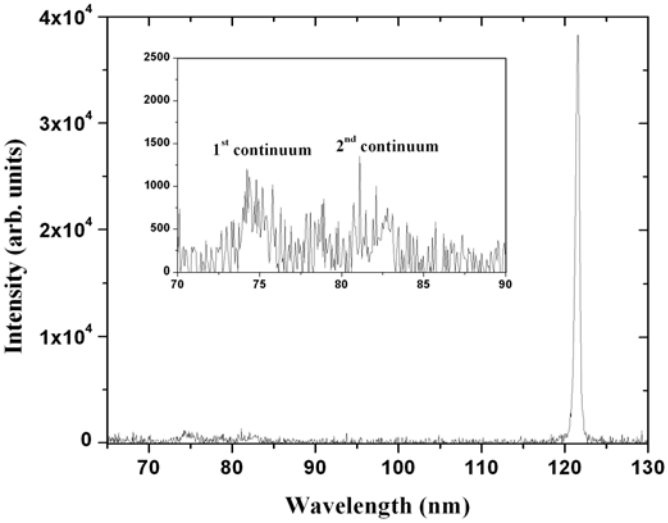

Fig. 18. The emission spectrum of a neon discharge with a small admixture of hydrogen (0.02%) at a total pressure of 500 Torr, a flow rate of 800 sccm and a net rf power of 30 W. The inset shows the expanded view of the spectrum in the 70–90 nm region.

As a function of pressure (at constant power of 30 W), the Lyman-α emission intensity was found to rise almost linearly up to a pressure of 200 Torr, where the intensity has its maximum. For higher pressures, the Lyman-α intensity decreases, but it still dominates the emission spectrum. The increase of the Lyman-α emission with increasing pressure follows the increase of the Ne_2^* second continuum intensity, which is the precursor of the Lyman-α emission, with pressure (see discussion above). The fact that the Lyman-α emission intensity reaches its maximum already at 200 Torr as compared to 400 Torr for the Ne_2^* second continuum can be explained by the fact that the peak emission intensity of the second continuum at 400 Torr was obtained in a pure Ne plasma. The addition of H_2 to the feed gas mixture essentially means introducing impurities, which will reduce the efficiency of excimer formation, e.g. by quenching the excimer precursors.

When the power was varied at constant pressure, we found that the intensity of the line emission increases monotonically as the power is increased. It is interesting to note that the Lyman-α intensity even increases for rf powers above 50 W, where the intensity of the second continuum as a function of rf power levels off (see discussion above). This may be explained by the fact that other mechanisms such as ionization of H_2 by Ne metastables followed by dissociative recombination or energy transfer from the Ne_2^* first excimer continuum may also contribute to the formation of H ($n = 2$) atoms in our plasma.

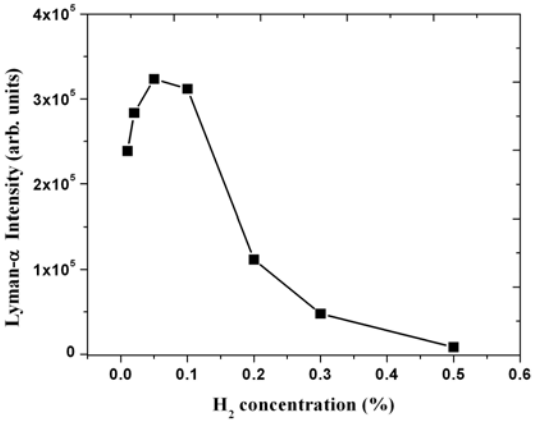

Fig. 19. The Lyman-α line intensity as a function of H_2 concentration at 200 Torr, 800 sccm flow rate and 30 W net rf power. The lines connecting the data points are just a guide to the eye.

The Lyman-α intensity increases with increasing H_2 concentration up to concentrations of 0.05% as shown by the data in Figure 19, which were obtained at a pressure of 200 Torr, a gas flow rate of 800 sccm, and a net rf power of 30 W. As the H_2 concentration is increased above 0.05%, the Lyman-α emission intensity begins to drop. At a H_2concentration of 0.5% the Lyman-α intensity has dropped to less than 3% of its peak value. A similar behavior was observed by Kurunczi et al. [8] in the case of the Lyman-α emission from a microhollow cathode discharge and was attributed to the increase in the H_2 density in the plasma at H_2 concentration about 0.05%. This causes (i) efficient quenching of the Ne metastables which reduces the formation of the Ne_2^* excimers and (ii) the formation of ground-state H atoms via dissociation of H_2, which cause self-absorption and trapping of the Lyman-α emission.

4.2.5 VUV emissions from a rf excited C-DBD plasma in an Ar–N_2 mixture

If a gaseous mixture of argon and a small amount of nitrogen (0.2% to 2.8%) is excited in the C-DBD discharge, more intense nitrogen emission appear in the spectrum as a result of the increase of the N_2 concentration and of energy transfer processes from excited argon species to nitrogen molecules and atoms. Under suitable pressure and N_2 concentration conditions, the nitrogen emissions become very intense. Strong atomic nitrogen line emissions in the VUV region have previously been observed in mixtures of argon with a small amount of nitrogen [76]. We studied the VUV emissions from a rf excited C-DBD plasma in Ar–N_2 mixtures at two different pressures, 50 Torr and 300 Torr. The objective was to investigate the influence of a controlled addition of N_2 to the argon discharge on possible energy transfer processes between the argon metastables and excimers to the atomic and molecular nitrogen in our source.

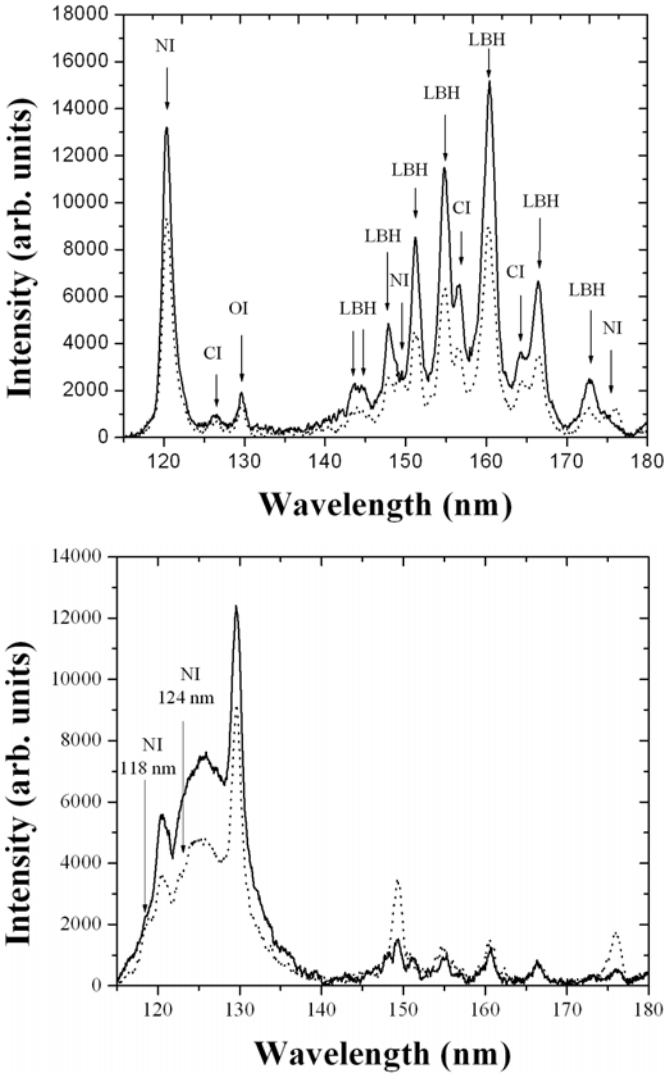

Fig. 20. Top: emission intensity from a Ar–N_2 discharge as a function of wavelength for two N_2 concentrations (0.2% (solid line) and 0.8% (dotted line)) at a pressure of 50 Torr, a power of 22 watts and a flow rate of 800 sccm; bottom: same at a pressure of 300 Torr emission intensity (0.2% N_2, solid line and 0.4% N_2, dotted line).

We recorded emission spectra obtained at five different N_2 concentrations between 0.2–2.8%. Figure 20 (top diagram) compares the emission spectra obtained at 0.2% and 0.8% N_2 admixture to Ar at a total pressure of 50 Torr, a total gas flow rate of 800 sccm, and a net rf power of 22 W. The emission is dominated by the NI atomic lines at the 120 nm $(2s^2 2p^2 3s)\ ^4\mathrm{P} \rightarrow (2s^2 2p^3)\ ^4\mathrm{S}^0$, the OI atomic line at 130 nm $2p^4\ ^3\mathrm{P} \rightarrow 2p^3 3s\ ^3\mathrm{S}^0$ and the emission of the molecular nitrogen LBH ($a\ ^1\Pi_g \rightarrow \mathrm{X}\ ^1\Sigma_g^+$) band between 140–175 nm. The intensity of all emissions decreases with increasing the N_2 concentration except for a small increase in the weak emission of the NI line at 149 nm $(2s^2 2p^2 3s)\ ^2\mathrm{P} \rightarrow (2s^2 2p^3)^2\mathrm{D}^0$. Figure 20 (bottom diagram) shows two spectra recorded at a higher pressure of 300 Torr and a N_2 admixture of 0.2%

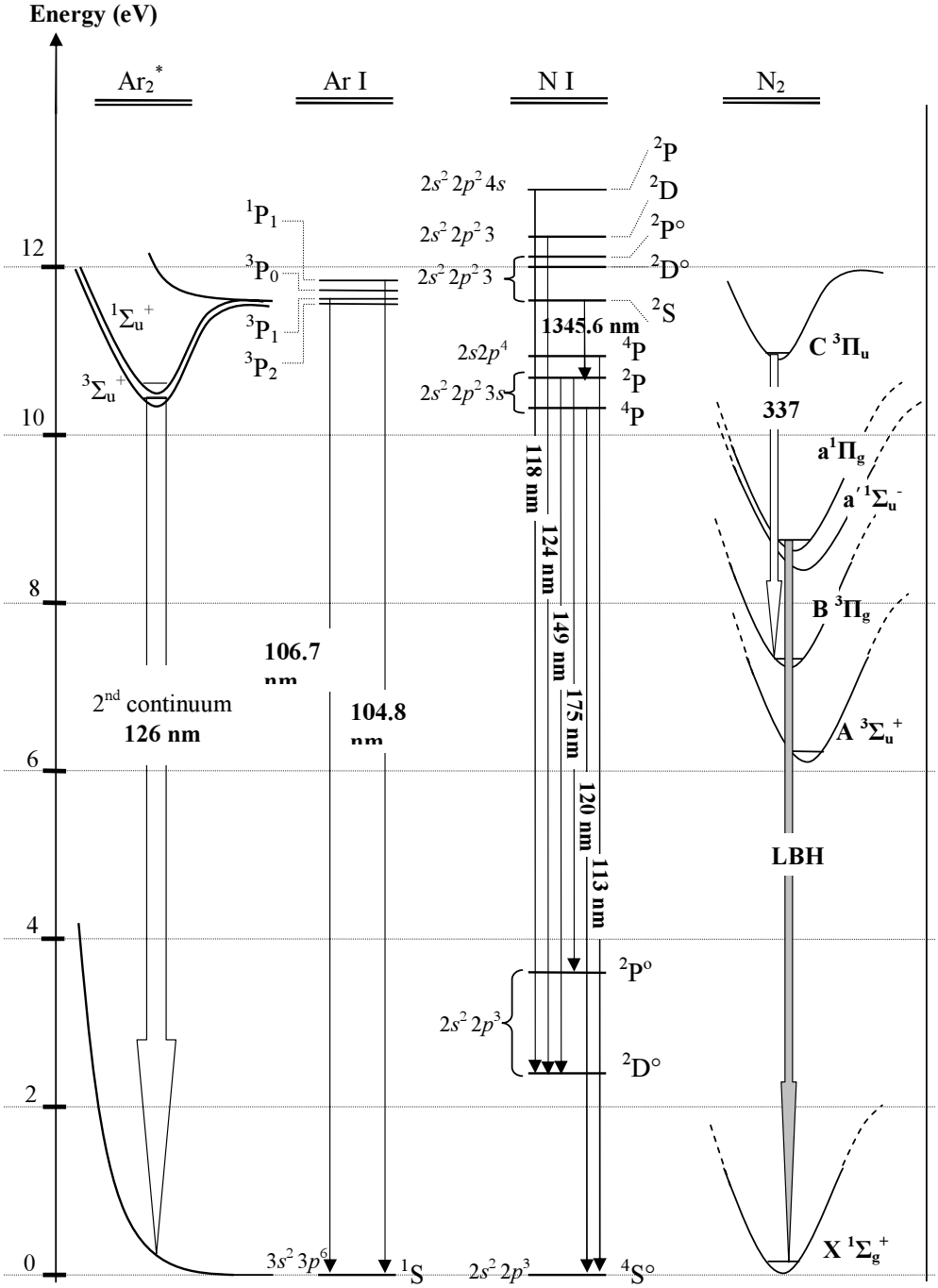

Fig. 21. Partial energy level diagram for the argon excimer, ArI, NI, and the N_2 molecule.

and 0.4%, respectively under otherwise identical operating conditions. We see a strong presence of the Ar_2^* second continuum at 126 nm in the spectra accompanied by the emission of an intense OI line at 130 nm. The emission intensities of the N_2 LBH bands and the NI line at 120 nm decrease significantly at the high pressure. We note that the Ar_2^* excimer emission and the OI emission are strongest at the lower N_2 concentration, whereas the emissions above 140 nm do not change much with varying N_2 concentration except for the two NI lines at 149 nm and 175 nm, which are stronger at the higher N_2 density.

In order to understand the experimental results depicted in Figure 20 and to elucidate the basic processes that cause the observed dependencies, it is illustrative to draw an energy diagram of the atomic and molecular levels for important the argon and nitrogen species as shown in Figure 21. The arrows indicate the possible transitions discussed in this work and their respective wavelengths. Gas mixtures containing Ar and a small admixture of N_2 in discharge plasmas have been widely studied [76–82]. However, there remain many observations that are difficult to explain in terms of the underlying basic processes [82].

Table 1. Rate constants (at 296 K) for nitrogen atom excitation by metastable argon [77].

Process	Rate constant (cm^3 $molecule^{-1}$ s^{-1})
$Ar^*(^3P_{2,0}) + N(^4S) \rightarrow N^*$ $(2s^2 2p^2 3s\ ^2P) + Ar(^1S_0)$	9.0×10^{-11}
$Ar^*(^3P_{2,0}) + N(^4S) \rightarrow N^*$ $(2s^2 2p^2 3s\ ^4P) + Ar(^1S_0)$	1.6×10^{-11}
Ar^* $(^3P_{2,0}) + N(^4S) \rightarrow N^*$ $(2s2p^4\ ^4P) + Ar(^1S_0)$	6.8×10^{-11}

As is well-known [84], the addition of even a small amount of N_2 to an Ar plasma changes the electron energy distribution function (eedf) of the plasma electrons. Argon has a deep Ramsauer minimum in the elastic scattering cross-section around 0.25 eV, where the cross-section dips to a value below 1×10^{-17} cm^2 [84] and the lowest-lying inelastic electron scattering channels require a minimum electron energy of well above 10 eV. N_2 has an elastic scattering cross-section which is almost 2 orders of magnitude higher at the electron energy where the Ramsauer minimum in Ar occurs [83] and the molecule has a pronounced peak in the inelastic electron scattering cross-section between about 1 and 5 eV with a maximum value of more than 1×10^{-15} cm^2 at 2.5 eV (largely due to vibrational excitation [83]). Thus, the major effect of introducing N_2 to an Ar plasma is a suppression of the high-energy tail of the electron energy distribution function (eedf), which causes a decrease in the electron temperature (however, we note that the concept of an electron temperature in a Ar–N_2 plasma should be used with caution in view of the highly non-Maxwellian eedf). Therefore, the rate of production of Ar metastables, Ar^m, and excited Ar atoms by electron impact from ground-state Ar atoms decreases with increasing N_2 content. The spectra in Figure 20 (top) suggest that — at a pressure of 50 Torr — the increase in N_2 number density, when the N_2 concentration is quadrupled from 0.2% to 0.8%, is not sufficient to compensate for the loss of energetic plasma electrons.

By contrast, the situation at 300 Torr (Fig. 20, bottom) is much more complex. The prominence of the Ar_2^* excimer emission indicates a significant presence of Ar metastables (Ar^m), the precursor to the Ar_2^* molecule. As a consequence, we need to consider collisional processes involving Ar^m and Ar_2^*. At the higher pressure, there is another channel that further reduces the density of Ar^m, quenching by N_2

$$Ar^m + N_2 \rightarrow N_2^* + Ar \tag{5}$$

where N_2^* represents all possible excited molecular N_2 states with energies below about 11.72 eV, the energy of the $Ar(^3P_o)$ metastables. The main quenching pathway in reaction (5) will result in the formation of $N_2^*(C\,^3\Pi_u)$ molecules, which emit the N_2 2nd positive system in the UV.

Energy transfer from both Ar metastables $Ar^*(^3P_{2,0})$ can efficiently excite three states in atomic nitrogen, the $(2s^2 2p^2 3s)$ ^2P state at 10.68 eV, the $(2s^2 2p^2 3s)$ ^4P state at 10.34 eV, and the $(2s2p^4)^4P$ state at 10.93 eV (as shown in Fig. 20). The $(2s^2 2p^2 3s)$ ^2P state at 10.68 eV is the upper state of both NI lines at 149 and 175 nm and the $(2s^2 2p^2 3s)$ ^4P state at 10.93 eV is the upper state for the emission of the NI line at 120 nm. The rate constants for the excitation of these states of atomic N by metastable argon taken from Piper et al. [77] are shown in Table 1. The rate constant for the first reaction in Table 1 is the highest which explains the prominence of the 149 and 175 nm NI line emissions at the higher pressure of 300 Torr, where the Ar^* density is relatively high. This observation is similar to what was reported by other authors [78]. Another process that can populate the $(2s^2 2p^2 3s)$ ^2P state is cascading from the $(2s^2 2p^2 3p)$ ^2S state at 11.60 eV, which can be efficiently populated by collisional energy transfer from $Ar(^3P_0)$ (11.72 eV) atoms (accompanied by radiative transitions 1345.6 nm) or via collisions with Ar atoms:

$$N(2s^2 2p^2 3p\ ^2S) \rightarrow N(2s^2 2p^2 3s\ ^2P) + h\nu(1345.6\text{ nm}) \tag{6}$$

$$N(2s^2 2p^2 3p\ ^2S) + Ar \rightarrow N(2s^2 2p^2 3s\ ^{2,4}P) + Ar. \tag{7}$$

This is followed by the emission of the NI lines at 120 nm, 149 nm, and 175 nm:

$$N(2s^2 2p^2 3s\ ^2P) \rightarrow N(2s^2 2p^3\ ^2D^0) + h\nu(149\text{ nm}) \tag{8}$$

$$N(2s^2 2p^2 3s\ ^2P) \rightarrow N(2s^2 2p^3\ ^2P^0) + h\nu(175\text{ nm}) \tag{9}$$

$$N(2s^2 2p^2 3s\ ^4P) \rightarrow N(2s^2 2p^3\ ^4S^0) + h\nu(120\text{ nm}). \tag{10}$$

Process (6) is important only at low pressures (<2 Torr). At all pressure used in this work (>50 Torr), process (7) is expected to be dominant.

Since the lifetime of the $N(2s^2 2p^2 3s\ ^2P)$ state is comparatively short (2 ns [78]), quenching processes at high pressure can be neglected for the 149 nm and 175 nm emission lines, but not for the 120 nm emission line. This explains the decrease of the intensity of the 120 nm line at higher pressure. The rate constant for the depopulation of the $N(2s^2 2p^2 3p\ ^2S)$ state by N_2 (36×10^{-11} $cm^3\,s^{-1}$) is larger than the depopulation rate by Ar ($25 \times 10^{-11} cm^3\,s^{-1}$) [78] by almost 50%. This fact and the large rate constant of the first reaction in Table 1 are among the main factors that contribute to the increase in the intensity of the 149 nm and 175 nm lines relative to the 120 nm line with increasing N_2 concentration, since the depopulation of the $N(2s^2 2p^2 3p\ ^2S)$ state increases the density of N atoms in the state that emits those two lines.

The processes above depend initially on the density of N atoms in the $(2s^2 2s^2 2p^2 3p)$ ^2S state. Thus, we will discuss the processes that populate this state in an attempt to explain the observed trends in the VUV emissions obtained from our discharge: the production of the atomic nitrogen lines in an Ar–N_2 mixture is related to the dissociation of N_2 molecules by electron impact of N_2 in the ground state and in the metastable A- and B-state

and to the vibrational excitation of the N_2 ground state molecules. Another channel to produce the atomic nitrogen lines is by charge transfer [79]

$$Ar^+ + N_2 \rightarrow N_2^+ + Ar \tag{11}$$

followed by dissociative recombination

$$N_2^+ + e \rightarrow N^m + N \tag{12}$$

where N^m denotes the metastable states in nitrogen. The rate coefficient for the above reactions are 1×10^{-11} $cm^3\,s^{-1}$ and, 2.6×10^{-7} $cm^3\,s^{-1}$ at 300 K, respectively [79]. Thus, the atomic nitrogen that is created in the last reactions is mainly in the ground ($^4S^0$) state and in the first excited (metastable) ($^2D^0$) state. As discussed in reference [79] atomic nitrogen can be produced efficiently from both Ar metastable states. The energy transfer from the $Ar^*(^3P_2)$ state (11.55 eV) to the $N(^4S^0)$ state with the excitation of the $(2s^22p^23s)$ ^2P states (10.68 eV) has a comparatively large rate coefficient of 9×10^{-11} $cm^3\,s^{-1}$ (see Tab. 1) despite the large energy gap between the two states. By contrast, the Ar^* ($^3P_1$) state (11.62 eV) has an energy that is essentially resonant with the $N(2s^22p^23p$ $^2S)$ state (11.60 eV).

Krylov et al. [79] also suggested the possibility of an efficient energy transfer from the $Ar_2^*(^3\Sigma_u^+)$ excimer state to atomic nitrogen in the first metastable $(2s^22p^3)$ $^2D^0$ state

$$Ar_2^*(^3\Sigma_u^+) + N^m(^2D^0) \rightarrow N^* + 2Ar^*(^1S_0). \tag{13}$$

The combined energy of the $Ar_2^*(^3\Sigma_u^+)$ excimers (9.84 eV) and the $N(^2D^0)$ metastables (2.38 eV) is 12.22 eV which is sufficient to excite the $(2s^22p^23p)$ $^2D^0$, $(2s^22p^23p)$ $^2P^0$, and $(2s^22p^23s)$ ^2D states. The first two states, via radiative cascading as mentioned above, are responsible for the 149 and 175 nm emissions. The energy difference between the third state and the metastable $(2s^22p^3)$ $^2D^0$ state is 9.98 eV which corresponds to the energy of photons emitted near the maximum of the Ar_2^* excimer continuum. Since the Ar_2^* molecules are only formed at high pressure, it is not surprising to see a high emission intensity of the NI line at 149 and 175 nm at higher pressure. What supports this notion is the appearance of a weak emission at 124 nm shown in Figure 20 (bottom), which can be attributed to the NI $(2s^22p^23s$ $^2D \rightarrow 2s^22p^3$ $^2D^0)$ transition at higher pressure as shown in Figure 21.

We expect that the $N_2(A\ ^3\Sigma_u^+)$ state is efficiently populated by electron impact [80,83]. Another route leading to the formation of $N_2(A\ ^3\Sigma_u^+)$ molecules in Ar–N_2 discharge plasmas is via collisional quenching of $N_2(B\ ^3\Pi_g$, $a'\ ^1\Sigma_u^-$ $a\ ^1\Pi_g)$ molecules by Ar atoms. The radiative and collisional coupling between the $N_2(A\ ^3\Sigma_u^+)$, $N_2(B\ ^3\Pi_g)$ and $N_2(C\ ^3\Pi_u)$ molecules is strongly influenced by the presence of Ar atoms in Ar–N_2 discharges because of the following reaction chain [81]:

$$\begin{aligned} N_2(a\ ^1\Pi_g) + Ar &\rightarrow N_2(a'\ ^1\Sigma_u^-) + Ar \\ &\rightarrow N_2(B\ ^3\Pi_g) + Ar \\ &\rightarrow N_2(A\ ^3\Sigma_u^+) + Ar. \end{aligned} \tag{14}$$

Quenching of $N_2(a'\ ^1\Sigma_u^-)$ and $N_2(a\ ^1\Pi_g)$ molecules as a result of the collision with Ar atoms populates the $N_2(B\ ^3\Pi_g)$ state. The subsequent quenching of this state in collisions with N_2 molecules and Ar atoms along with its radiative decay populate the $N_2(A\ ^3\Sigma_u^+)$ state [81]. As a result, quenching of the $N_2(a\ ^1\Pi_g)$ state (the emitting state of the LBH bands) explains the disappearance of the LBH bands in our spectra in Ar–N_2 mixtures at high pressure, since the collision frequency increases with pressure and because of the relatively long radiative lifetime of the $a\ ^1\Pi_g$ state (1.15×10^{-4} s) [80]. The decrease in the emission intensity of the LBH bands with increasing N_2 concentration is attributed to an increase in the frequency of collisions which quench the LBH bands.

The $N_2(A\ ^3\Sigma_u^+)$ state is mainly responsible for populating the $N(2s^2\ 2p^3\ ^2P^0)$ level through the reaction

$$N_2(A\ ^3\Sigma_u^+) + N(^4S^0) \rightarrow N_2(X\ ^1\Sigma) + N(^2P^0) \tag{15}$$

followed by electron impact excitation of $N(^2P^0)$. Furthermore, argon metastables can selectively populate higher excited states of nitrogen, $N_2(C\ ^3\Pi_u)$ and $N_2(B\ ^3\Pi_g)$ by two-body collisions. These states cascade radiatively to the $N_2(A\ ^3\Sigma_u^+)$ level [27,84]. Thus, the atomic nitrogen that is created in the last reaction is mainly in the (metastable) $(2s^22p^3)$ $^2P^0$ state. Here, we suggest another energy transfer process that involves the Ar_2^* second excimer continuum (9.84 eV) and the N $(2s^22p^3$ $^2P^0)$ (3.57 eV) metastable state to produce N atoms in the $(2s^22p^24s$ $^2P)$ state (13 eV). This notion is supported by the NI emission around 118 nm at 300 Torr shown in Figure 20 (bottom). We attribute this emission to the $(2s^22p^2$ $4s)$ $^2P \rightarrow (2s^22p^3)$ $^2D^\circ$ transition (Fig. 21).

5 Summary

High-pressure plasmas in pure rare gases and in gas mixtures of rare gases with molecular gases such as H_2 and N_2 are efficient sources of VUV and UV radiation such as excimer emissions, intense atomic line emissions and molecular band emissions. Spectroscopic studies of the VUV and UV emissions from these plasmas can be used to elucidate the underlying collisional and radiative processes that lead to these emissions and that determine their dependence on the plasma operating parameters (such as pressure, power, mode of excitation, etc.). Spectroscopic studies can also serve to determine important plasma parameters such as the translational (gas), rotational, and vibrational temperature of the plasma species. The present article summarizes selected results obtained recently in high-pressure microhollow cathode discharge, capillary plasma electrodes discharge, and cylindrical dielectric barrier discharge plasmas in Ne, Ar, Ne–H_2, Ne–N_2, and Ar–N_2 gas mixtures.

The work described in this paper has bee supported by the U.S. National Science Foundation, the U.S. Air Force Office of Scientific Research, and the U.S. Army Research Office through

a DURIP Award. One of us (KM) is also grateful for the support from the William Paterson University Assigned Release Program. We would like to thank Prof. N. Abramzon, Dr. P. Kurunczi, Mr. J. Lopez, Mr. W. Zhu, and Ms. M Figus for their contributions to parts of the results reported here as well as for their many useful suggestions and for helpful discussions.

References

1. See e.g. *Non-Equilibrium Air Plasmas at Atmospheric Pressure*, edited by K. Becker, U. Kogelschatz, K. Schoenbach, R. Barker (IOP Publ., Bristol, UK, 2005), Chap. 9
2. Y. Raizer, *Gas Discharge Physics* (Springer Verlag, Heidelberg, 1991)
3. E.E. Kunhardt, IEEE Trans. Plasma Sci. **28**, 1 (2000)
4. K. Becker, P. Kurunczi, K.H. Schoenbach, Phys. Plasmas **9**, 2399 (2002)
5. D. Dietz, S. Wieman, T. Chou, T.L. Su, O. Mogzina, C. Christodoulatos, G. Korfiatis, P.J. Ricatto, E. Houston, K. Becker, *56th Gaseous Electronics Conference*, San Francisco, CA (2003); D. Dietz, S. Wieman, T. Chou, T.L. Su, O. Mogzina, C. Christodoulatos, G. Korfiatis, P.J. Ricatto, E. Houston, K. Becker, Bull. Am. Phys. Soc. **48**, 64 (2003)
6. D. Dietz, H. Ghezel-Ayagh, J. Hunt, A. Belkind, K. Becker, A. Nickens, *31st IEEE ICOPS*, Baltimore, MD (2004), p. 413
7. H. Qiu, K. Martus, W.Y. Lee, K. Becker, Int. J. Mass Spectrom. **233**, 19 (2004)
8. A. Koutsospyros, S.-M. Yin, C. Christodoulatos, K. Becker, Int. J. Mass Spectrom. **233**, 305 (2004)
9. N.S. Panikov, S. Paduraru, R. Crowe, P.J. Ricatto, C. Christodoulatos, K. Becker, IEEE Trans. Plasma Sci. **30**, 1424 (2002)
10. L. Moskwinski, P.J. Ricatto, N. Abramzon, K. Becker, G. Korfiatis, C. Christodoulatos, in *Proc. IV. Symposium on Applications of Plasma Processes* (SAPP), Jasna, Slovakia (2003), p. 17
11. K.H. Schoenbach, R. Verhappen, T. Tessnow, F.E. Peterkin, W. Byszewski, Appl. Phys. Lett. **68**, 13 (1996)
12. A.D. White, J. Appl. Phys. **30**, 711 (1959)
13. K.H. Schoenbach, A. El-Habachi, W. Shi, M. Ciocca, Plasma Sources Sci. Technol. **6**, 468 (1997)
14. A. Fiala, L.C. Pitchford, J.P. Boeuf, Contr. Papers, *XXII Conf. on Phenomena in Ionized Gases*, Hoboken, NJ, 1995, p. 191
15. D.J. Sturges, H.J. Oskam, J. Appl. Phys. **35**, 2887 (1964)
16. H. Helm, Z. Naturforsch. **27a**, 1812 (1972)
17. J.P. Boeuf, L.C. Pitchford, K.H. Schoenbach, Appl. Phys. Lett. **86**, 71501 (2005)
18. T. Paul, R. Hartmann, J. Heberlein, K.H. Schoenbach, W. Shi, R. Stark, *Proc. International Thermal Spray Conference*, edited by E. Lugscheider, ASM International, Materials Park, Ohio, pp. 793-796, 2002
19. Abdel-Aleam H. Mohamed, R. Block, K.H. Schoenbach, IEEE Trans. Plasma Sci. **30**, 182 (2002)
20. R.H. Stark, K.H. Schoenbach, J. Appl. Phys. **89**, 3568 (2001)
21. E.E. Kunhardt, K. Becker, US Patents 5872426, 6005349, and 6147452.
22. S. Okazaki, M. Kogoma, M. Uehara, Y. Kimura, J. Phys. D **26**, 889 (1993)
23. E.E. Kunhardt, K. Becker, L. Amorer, *Proc. 12th International Conference on Gas Discharges and their Applications*, Greifswald, Germany, 1997, p. I-374
24. E.E. Kunhardt, K. Becker, L. Amorer, L. Palatini, Bull. Am. Phys. Soc. **42**, 1716 (1997)
25. L.E. Amorer, Ph.D. thesis, Stevens Institute of Technology (1999), unpublished
26. E.E. Kunhardt, private communication
27. B. Eliasson, U. Kogelschatz, IEEE Trans. Plasma Sci. **19**, 309 (1991); see also *Non-Equilibrium Air Plasmas at Atmospheric Pressure*, edited by K. Becker, U. Kogelschatz, K. Schoenbach, R. Barker (IOP Publ., Bristol, UK, 2005), Chap. 6
28. M. Laroussi, in *Proc. IEEE Int. Conf. Plasma Sci.,* Monterey, CA (1999), p. 203
29. N. Masoud, K. Martus, K. Becker, Int. J. Mass Spectrom. **233**, 395 (2004)
30. N. Masoud, K. Martus, M. Figus, K. Becker, Contr. Plasma Phys. **45**, 30 (2005)
31. N. Masoud, K. Martus, K. Becker, J. Phys. D **38**, 1674 (2005)
32. P. Kurunczi, J. Lopez, H. Shah, K. Becker, Int. J. Mass Spectrom. **205**, 277 (2001)
33. P. Kurunczi, K.E. Martus, K. Becker, Int. J. Mass Spectrom. **223/224**, 37 (2003)
34. P. Kurunczi, M. Moshely, K.H. Schoenbach, K. Becker, in *Spectroscopy of Non-Equilibrium Plasmas at Elevated Temperatures*, edited by V.N. Ochkin, SPIE Proceedings, Vol. 4460 (SPIE Press, Bellingham, WA, USA), p. 239
35. J.K. Rice, A.W. Johnson, J. Chem. Phys. **63**, 5235 (1975)
36. J.L. Delcroix, C.M. Ferreira, A. Ricard, "Metastable Atoms in Ionized Gases", in *Principles of Gas Lasers*, editde by G. Belufi (Wiley Publ., New York, 1976)
37. M. Moselhy, R.H. Stark, K.H. Schoenbach, U. Kogelschatz, Appl. Phys. Lett. **78**, 880 (2001)
38. M. Moselhy, I. Petzenhauser, K. Frank, K.H. Schoenbach, J. Phys. D: Appl. Phys. **36**, 2922 (2003)
39. A. El-Habachi, K.H. Schoenbach, Appl. Phys. Lett. **73**, 885 (1998)
40. K.H. Schoenbach, A. El-Habachi, M.M. Moselhy, W. Shi, R.H. Stark, Phys. Plasmas **7**, 2186 (2000)
41. A. El-Habachi, W. Shi, M. Moselhy, R.H. Stark, K.H. Schoenbach, J. Appl. Phys. **88**, 3220 (2000)
42. A. El-Habachi, K.H. Schoenbach, Appl. Phys. Lett. **72**, 22 (1998).
43. K.H. Schoenbach, M. Moselhy, W. Shi, R. Bentley, Vac. Sci. Technol. A **21**, 1260 (2003)
44. M. Moselhy, W. Shi, R. H. Stark, K.H. Schoenbach, IEEE Trans. Plasma Science **30**, 198 (2002)
45. M. Moselhy, W. Shi, R.H. Stark, K.H. Schoenbach, Appl. Phys. Lett. **79**, 1240 (2001)
46. C.O. Laux, C.H. Kruger, J. Quant. Spectroscop. Radiat. Transfer **48**, 9 (1992)
47. T. Nozaki, Y. Unno, Y. Miyazaki, K. Okazaki, *15th International Symposium on Plasma Chemistry*, Orleans, France, (2001), Vol. 1, pp. 77-83
48. G. Herzberg, *Molecular Spectra and Molecular Structure*, (Van Nostrand-Reinhold, New York, 1950), Vol. 1
49. S. Cheskis, A. Kachanov, M. Chenevier, F. Stoeckel, Appl. Phys. B **64**, 713 (1997)

50. P. Kurunczi, N. Abramzon, M. Figus, K. Becker, Acta Phys. Slov. **54**, 115 (2004)
51. S.V. Pancheshnyi, S.M. Starikovkaia, A.Yu. Starikovskii, Chem. Phys. Lett. **294**, 523 (1998)
52. P.G. Kistemaker, A.E. de Vries, Chem. Phys. **7**, 371 (1975)
53. E. Stoffels, A.J. Flikweert, W.W. Stoffels, G.M.W. Kroesen, Plasma Sources Sci. Technol. **11**, 383 (2002)
54. V.M. Donnelly, M.V. Malyshev, Appl. Phys. Lett. **77**, 2467 (2000)
55. A. Lofthus, P. Krupenie, J. Phys. Chem. Ref Data **6**, 1 (1977)
56. G. Hartmann, P.C. Johnson, J. Phys. B: At. Mol. Phys. **11**, 1597 (1978)
57. R.W. Nicholls, J. Res. Nat. Bur. Stand. A. Phys. Chem. **65A**, 451 (1961)
58. N. Nur, J.L. Hernandez, N. Bonifaci, A. Dent, A.A. Belevtsev, Conference Record of the ICDL 96, *12th International Conference of Conduction and Breakdown in Dielectric Liquid*, Roma, Italy, July 15-19 (1996)
59. I.I. Sobelman, *Atomic Spectra and Radiative Transitions* (Springer Verlag, Heidelberg, 1979)
60. K. Bartschat, D.H. Madison, J. Phys. B: At. Mol. Phys. **20**, 5839 (1987)
61. I. Kanik, J.M. Ajello, G.K. James, J. Phys B: At. Mol. Opt. Phys. **29**, 2355 (1996)
62. P.K. Leichner, Phys. Rev. A **8**, 815 (1973)
63. W. Krotz, A. Ulrich, B. Busch, G. Ribitzki, J. Wieser, Appl. Phys. Lett. **55**, 2265 (1989)
64. P. Kurunczi, H. Shah, K. Becker, J. Phys. B: At. Mol. Opt. Phys. **32**, L651 (1999)
65. B. Eliasson, M. Hirth, U. Kogelschatz, J. Phys. D: Appl. Phys. **20**, 1421 (1987)
66. T. Grieget, H.W. Drotleff, J.W. Hammer, K. Petkau, J. Chem. Phys. **93**, 4581 (1990)
67. H. Langhoff, Opt. Comm. **68**, 31 (1988)
68. A.K. Amirov, O.V. Korshounov, V.F Chinnov, J. Phys. B **27**, 1753 (1994)
69. See e.g. M. McCusker, "The Rare Gas Excimers", in *Excimer Lasers*, edited by C.K. Rhodes (Springer-Verlag, Heidelberg, 1984) and references therein to earlier publications; as discussed in this article, the radiative lifetime of the $Ne_2^*(^3\Sigma_u)$ excimer state has been measured by several authors who report values ranging from 5.1 μs to 12 μs with an average value of 8.9 μs which has an estimated uncertainty of no less than about 30%
70. M.R. Wertheimer, A.C. Fozza, A. Hollander, Nucl. Instrum. Meth. Phys. Res. B **151**, 65 (1999)
71. N. Merbahi, N. Sewraj, F. Marchal, Y. Salamero, P. Millet, J. Phys. D: Appl. Phys. **37**, 1664 (2004)
72. A. El-Dakrouri, J. Yan, M.C. Gupta, M. Laroussi, Y. Badr, J. Phys. D: Appl. Phys. **35**, L109 (2002)
73. Ch. A. Brau, "Rare Gas Halogen Excimers", in *Excimer Lasers*, edited by C.K. Rhodes (Springer Verlag, Berlin, Heidelberg, New York, 1984)
74. J. Wieser, M. Salvermoser, L.H Shaw, D. E. Murnick, H. Dahi, J. Phys. B: At. Mol Opt Phys. **31**, 4589 (1998)
75. P. Kurunczi, Ph.D. thesis, Stevens Institute of Technology (2003), unpublished
76. W.T. Rawlins, L.G. Piper, SPIE **279**, 58 (1981)
77. L.G. Piper, M.A. Clyne, P.B. Monkhouse, Chem. Phys. **51**, 107 (1980)
78. H. Umemoto, N. Terada, K. Tanaka, S. Oguro, Phys. Chem. Chem. Phys. **2**, 3425 (2000)
79. B. Krylov, A. Morozov, G. Gerasimov, A. Arnesen, R. Hallin, F. Heijkenskjöld, J. Phys. B: At. Mol. Opt. Phys. **35**, 4257 (2002)
80. A. Rahman, A.P. Yalin, V. Surla, O. Stan, K. Hoshimiya, Z. Yu, E. Littlefield, G.J. Collins, Plasma Sources Sci. Technol. **13**, 537 (2004)
81. C.M. Ferreira, E. Tatarova, V. Guerra, B.F. Gordiets, J. Henriques, F.M. Dias, M. Pinheiro, IEEE Tran. Plasma Sci. **31**, 645 (2003)
82. T. Kimura, K. Akatsuka, K. Ohe, J. Phys. D: Appl. Phys. **27**, 1664 (1994)
83. See e.g. K. Becker, M. Schmidt, "Plasma Chemistry" in *Encyclopedia of Chemical Physics and Physical Chemistry*, edited by J.H. Moore, N.D. Spencer (Institute of Physics Publishing, London, 2002), p. 2491, and references therein to earlier publications
84. A. Zecca, G.P. Karwasz, R.S. Brusa, Riv. Nuovo Cim. **19**, 1 (1996)